What ingredients are on our hands?

For calorimeter and a large detector for high-energy e^+e^- colliers

Sehwook Lee (Kyungpook National University)
KFCC brainstorming workshop
Hilton Gyeongju, Nov. 12, 2021

Dual-Readout Calorimetry

20-year generic calorimeter R&D

- 1986-1992: the secrets of compensation were unraveled
- CALOR 1997, Tucson, USA: Dual-Readout calorimeter was proposed
- 35 papers for 20 years
  - We joked we produced the largest number of papers per particle

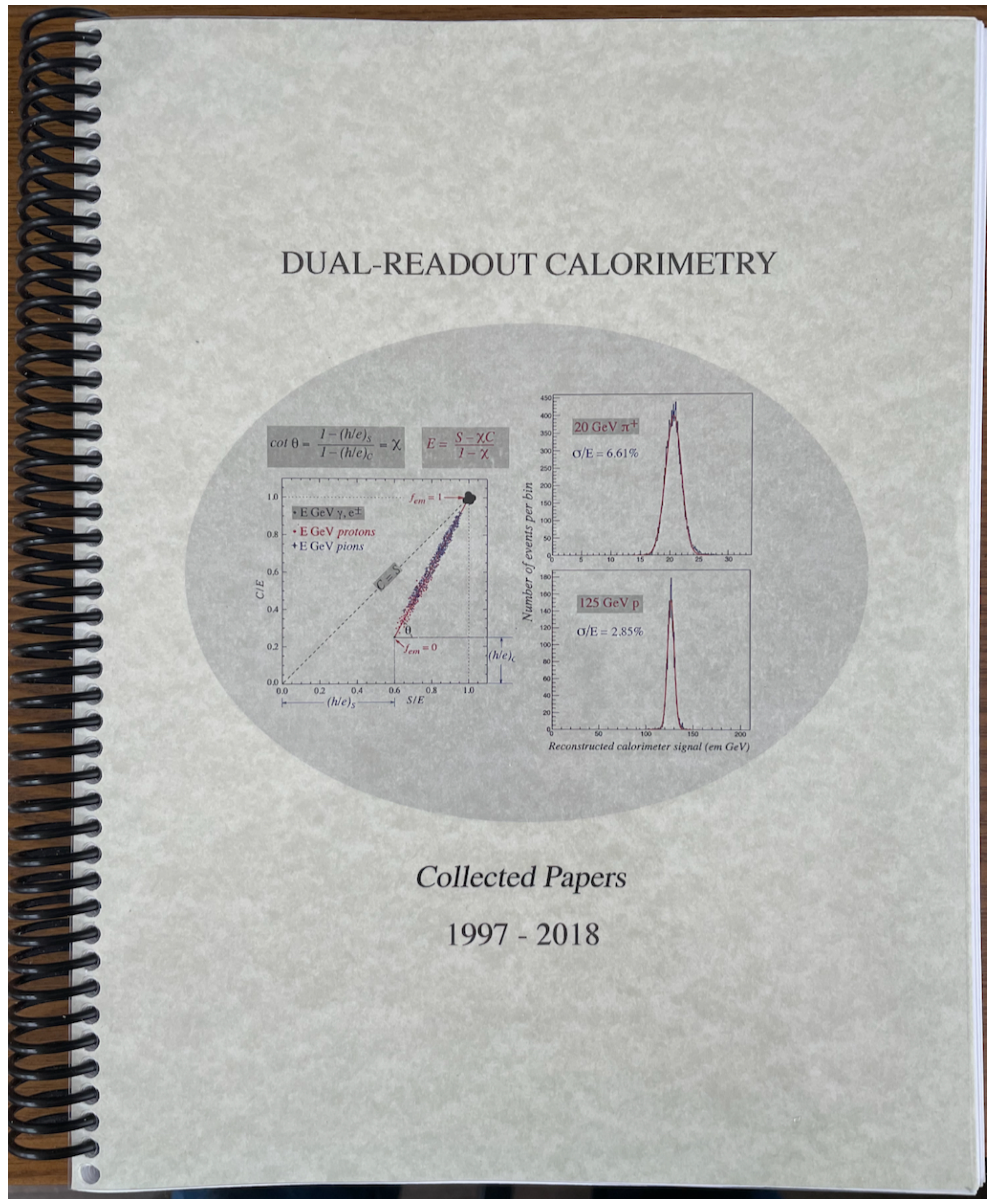

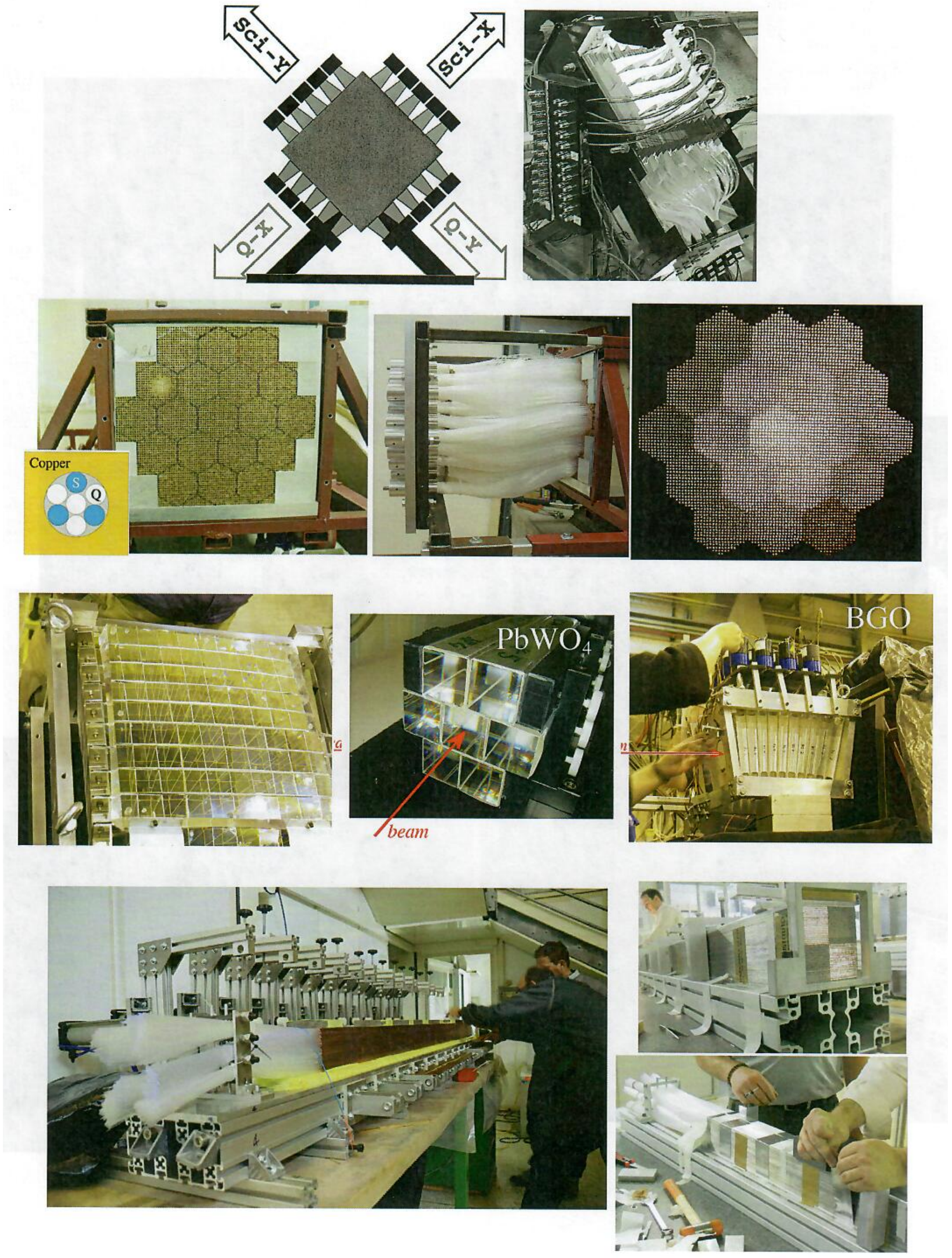

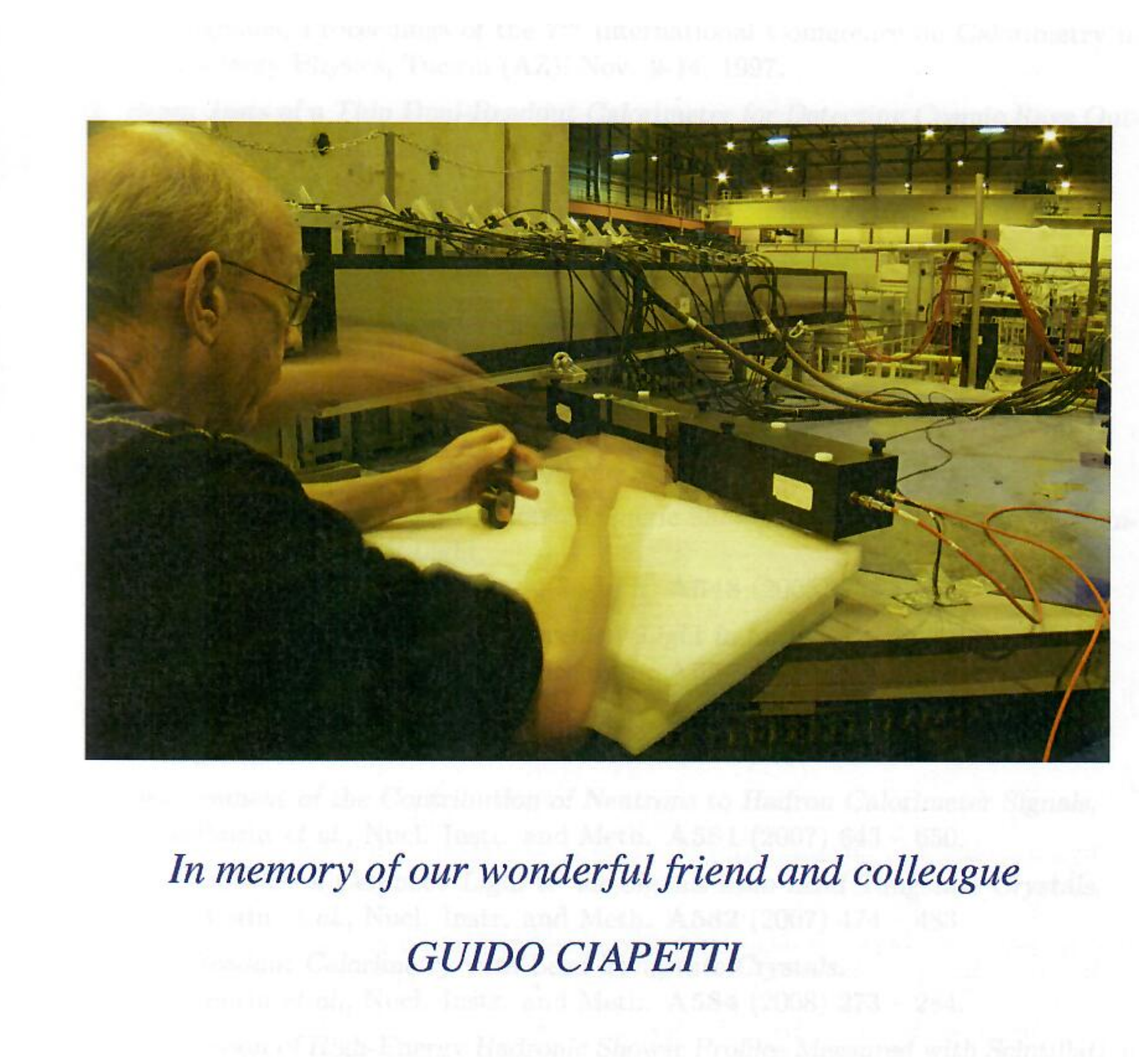

RD52 Collaboration (2010-2018)

[35] S. Lee, M. Livan, R. Wigmans, Dual-Readout Calorimetry, Rev. Mod. Phys. 90 (2018) 025002.

[34] Sehwook Lee, John Hauptman, Richard Wigmans, Where the energy goes?, 2018 Physics World Focus on Instruments and Vacuum, August 2018

[33] M. Antonello, et al, Tests of a dual-readout fiber calorimeter with SiPM light sensors, Nucl. Instr. and Meth. in Phys. Res. A 899 (2018) 52.

[32] S. Lee, M. Livan, R. Wigmans, On the limits of the hadronic energy resolution of calorimeters, Nucl. Instr. and Meth. in Phys. Res. A 882 (2018) 148.

[31] S. Lee, et al., Hadron detection with a dual-readout fiber calorimeter, Nucl. Instr. and Meth. in Phys. Res. A 866 (2017) 76.

[30] R. Wigmans, New results from the RD52 project, Nucl. Instr. and Meth. in Phys. Res. A 824 (2016) 721.

[29] A. Cardini, et al., The small-angle performance of a dual-readout fiber calorimeter, Nucl. Instr. and Meth. in Phys. Res. A 808 (2016) 41.

[28] N. Akchurin, et al., Lessons from Monte Carlo simulations of the performance of a dual-readout fiber calorimeter, Nucl. Instr. and Meth. in Phys. Res. A 762 (2014) 100.

[27] N. Akchurin, et al., Particle identification in the longitudinally unsegmented RD52 calorimeter, Nucl. Instr. and Meth. in Phys. Res. A 735 (2014) 120.

[26] N. Akchurin, et al., The electromagnetic performance of the RD52 fiber calorimeter, Nucl. Instr. and Meth. in Phys. Res. A 735 (2014) 130.

[25] N. Akchurin, et al., Detection of electron showers in Dual-Readout crystal calorimeters, Nucl. Instr. and Meth. in Phys. Res. A 686 (2012) 125.

[24] N. Akchurin, et al., A comparison of BGO and BSO crystals used in the dual-readout mode, Nucl. Instr. and Meth. A 640 (2011) 91.

[23] N. Akchurin, et al., Polarization as a tool for dual-readout calorimetry, Nucl. Instr. and Meth. A 638 (2011) 47.

[22] Gabriella Gaudio, New result from the DREAM project, Nucl. Instr. and Meth. A 628 (2011) 339.

[21] N. Akchurin, et al., Optimization of crystals for applications in dual-readout calorimetry, Nucl. Instr. and Meth. A 621 (2010) 212.

[20] R. Wigmans, The DREAM project - Towards the ultimate in calorimetry, Nucl, Instr. and Meth. A 617 (2010) 129.

DREAM (Dual-REAdout Method) Collaboration (?-2009)

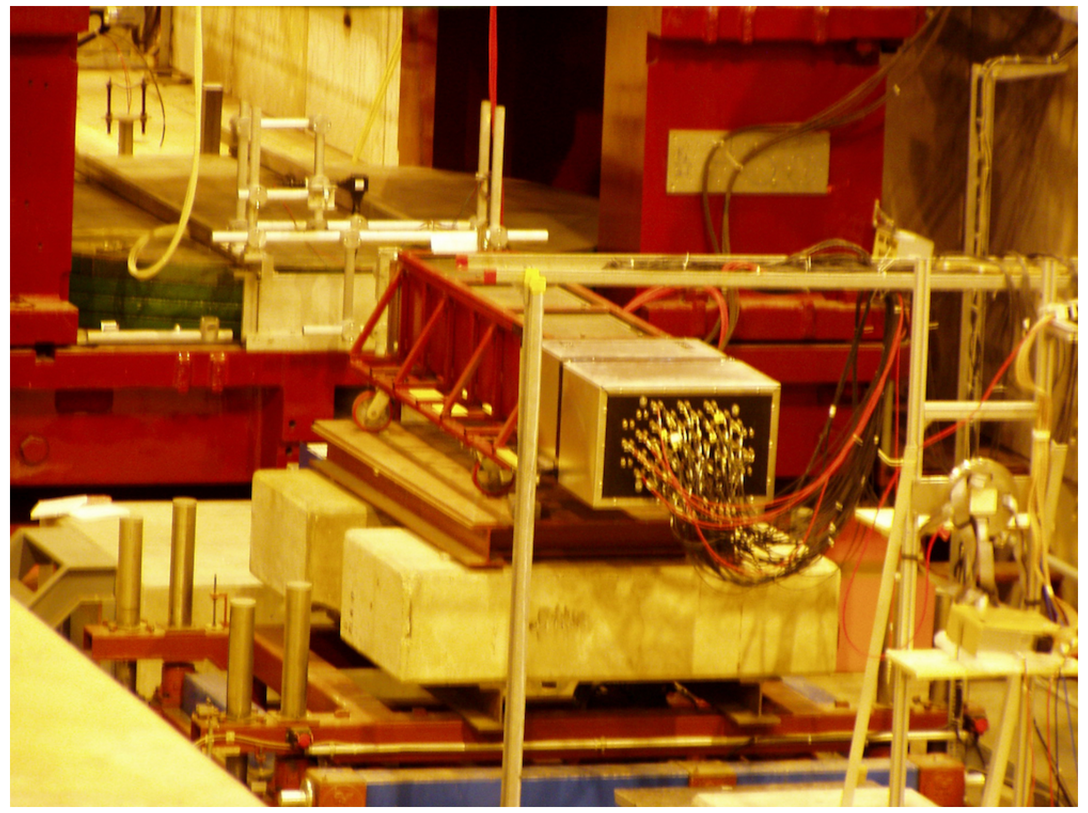

[19] N. Akchurin, et al., Dual-readout calorimetry with a full-size BGO electromagnetic section, Nucl. Instr. and Meth. A 610 (2009) 488.

[18] N. Akchurin, et al., New crystals for dual-readout calorimetry, Nucl. Instr. and Meth. A 604 (2009) 512.

[17] N. Akchurin, et al., Dual-Readout Calorimetry with Crystal Calorimeters, Nucl. Instr. and Meth. A 598 (2009) 710.

[16] N. Akchurin, et al., Neutron Signals for Dual-Readout Calorimetry, Nucl. Instr. and Meth. A 598 (2009) 422.

[15] M. Nikl et al., Luminescence and scintillation characteristics of heavily Pr^{3+}-doped PbWO4 single crystals, Journal of Applied Physics 104, (2008) 093514.

[14] N. Akchurin, et al., Separation of crystal signals into scintillation and Cherenkov components, Nucl. Instr. and Meth. A 595 (2008) 359.

[13] N. Akchurin, et al., Effects of the temperature dependence of the signals from lead tungstate crystals, Nucl. Instr. and Meth. A 593 (2008) 530.

[12] N. Akchurin, et al., Comparison of High-Energy Hadronic Shower Profiles Measured with Scintillation and Cerenkov Light, Nucl. Instr. and Meth. A 584 (2008) 304.

[11] N. Akchurin, et al., Dual-Readout Calorimetry with Lead Tungstate Crystals, Nucl. Instr. and Meth. A 584 (2008) 273.

[10] N. Akchurin, et al., Contributions of Cherenkov light to the signals from lead tungstate crystals, Nucl. Instr. and Meth. A 582 (2007) 474.

[9] N. Akchurin, et al., Measurement of the Contribution of Neutrons to Hadron Calorimeter Signals, Nucl. Instr. and Meth. A 581 (2007) 643.

[8] R. Wigmans, The DREAM project-Results and plans, Nucl. Instr. and Meth. A 572 (2007) 215.

[7] N. Akchurin, et al., Separation of Scintillation and Cerenkov Light in an Optical Calorimeter, Nucl. Instr. and Meth. A 550 (2005) 185.

[6] N. Akchurin, et al., Comparison of High-Energy Electromagnetic Shower Profiles Measured with Scintillation and Cerenkov Light, Nucl. Instr. and Meth. A 548 (2005) 336.

[5] N. Akchurin, et al., Hadron and jet detection with a dual-readout calorimeter, Nucl. Instr. and Meth. A 537 (2005) 537.

[4] N. Akchurin, et al., Electron detection with a dual-readout calorimeter, Nucl. Instr. and Meth. A 536 (2005) 29.

[3] N. Akchurin, et al., Muon detection with a dual-readout calorimeter, Nucl. Instr. and Meth. A 533 (2005) 305.

[2] Richard Wigmans, Status and perspectives of detectors for experiments in HEP and related fields, Nucl. Instr. and Meth. A 518 (2004) 9.

[1] Vladimir Nagaslaev, Alan Sill, Richard Wigmans, Beam tests of a thin dual-readout calorimeter for detecting cosmic rays outside the Earth's atmosphere, Nucl. Instr. and Meth. A 462 (2001) 411

Proposal (1997)

[0] Richard Wigmans (Texas Tech. University, USA), Quartz Fibers and the Prospects for Hadron Calorimetry at the 1% Resolution Level, CALOR 1997 Tucson, USA

1997
CALOR 1997, Tucson, USA

- Quartz Fibers and the Prospects for Hadron Calorimetry at the 1% Resolution Level
- Richard Wigmans proposed a fiber calorimeter consisting of scintillating and quartz fibers
  - Scintillating fibers: the visible energy
  - Quartz fibers: the em energy

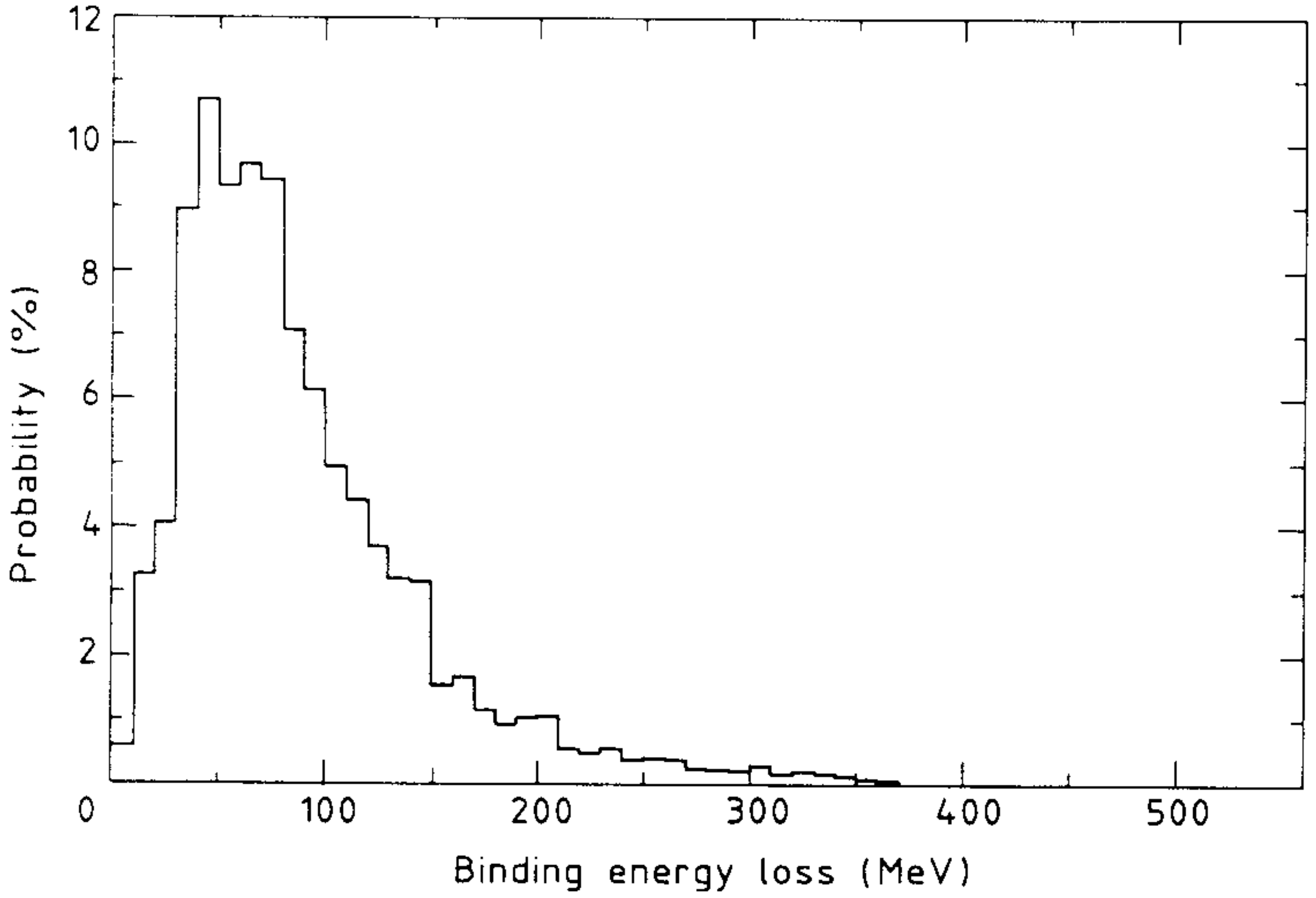

Figure 4: The nuclear binding energy lost in spallation reactions induced by 1 GeV pions on ^{63}Cu nuclei.

2001
[1] NIM A 462 (2001) 411-425

- Beam tests of a thin dual-readout calorimeter for detecting cosmic rays outside the Earth’s atmosphere

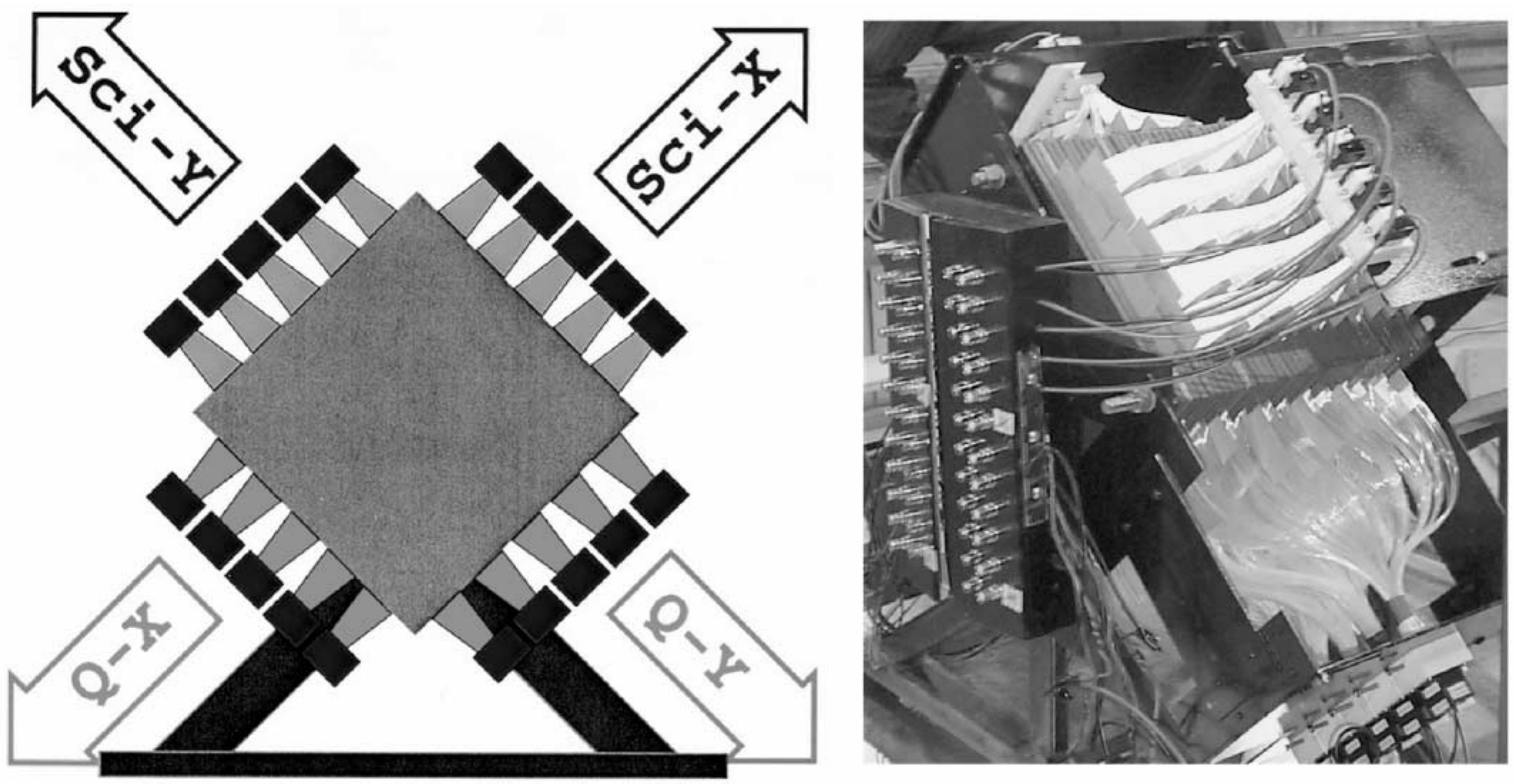

Fig. 1. Schematic layout and a photograph of the dual-readout calorimeter. Thin lead plates are interleaved with 4 cm wide ribbons of scintillating and quartz fibers, which both provide readout in two coordinates.

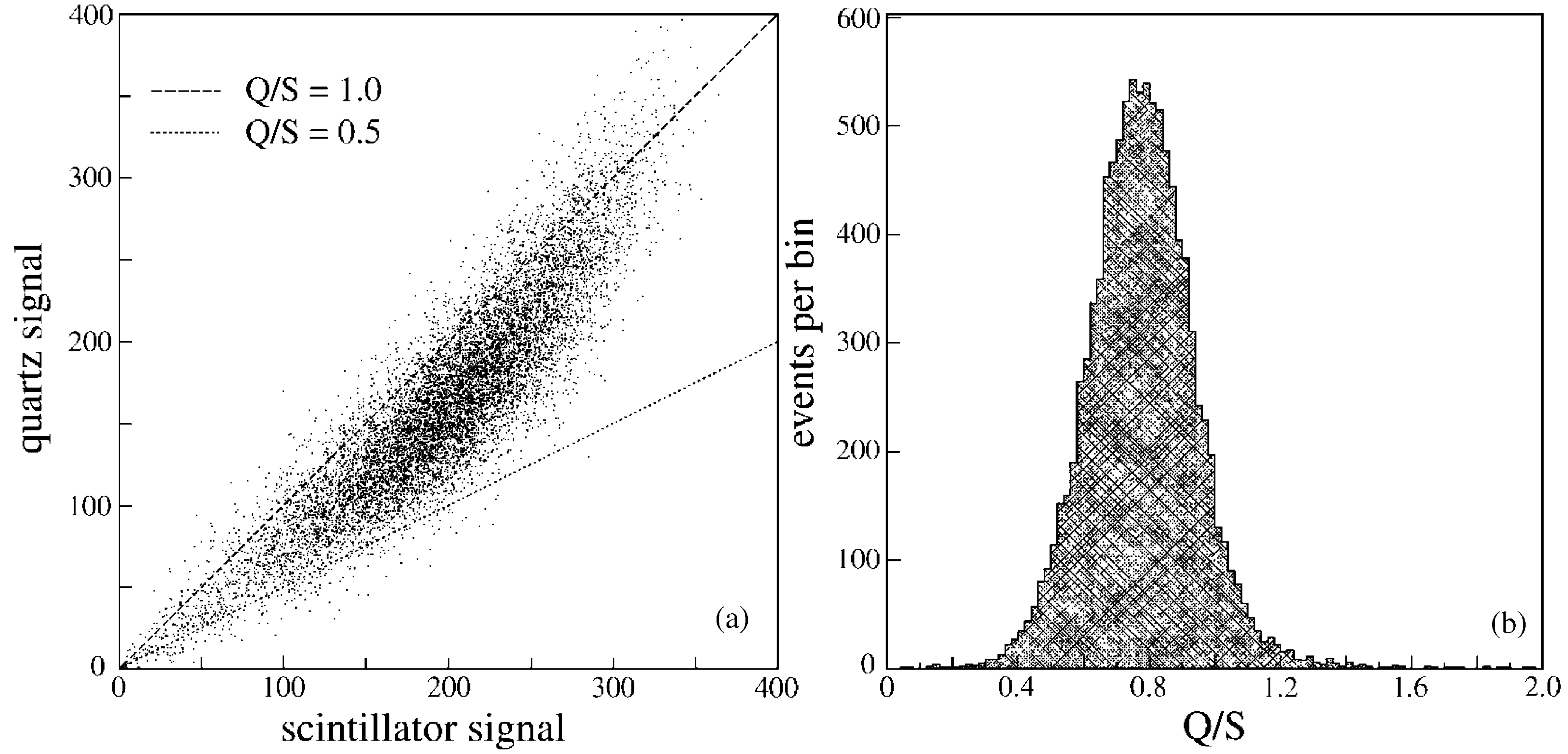

Fig. 8. Results of tests of the dual-readout calorimeter with 375 GeV pions. Scatter plot of the signals recorded in the quartz fibers v
those in the scintillating fibers (a). Distribution of the ratio of the signals observed in the quartz fibers and the scintillating fibers (b

Prototype DREAM Module

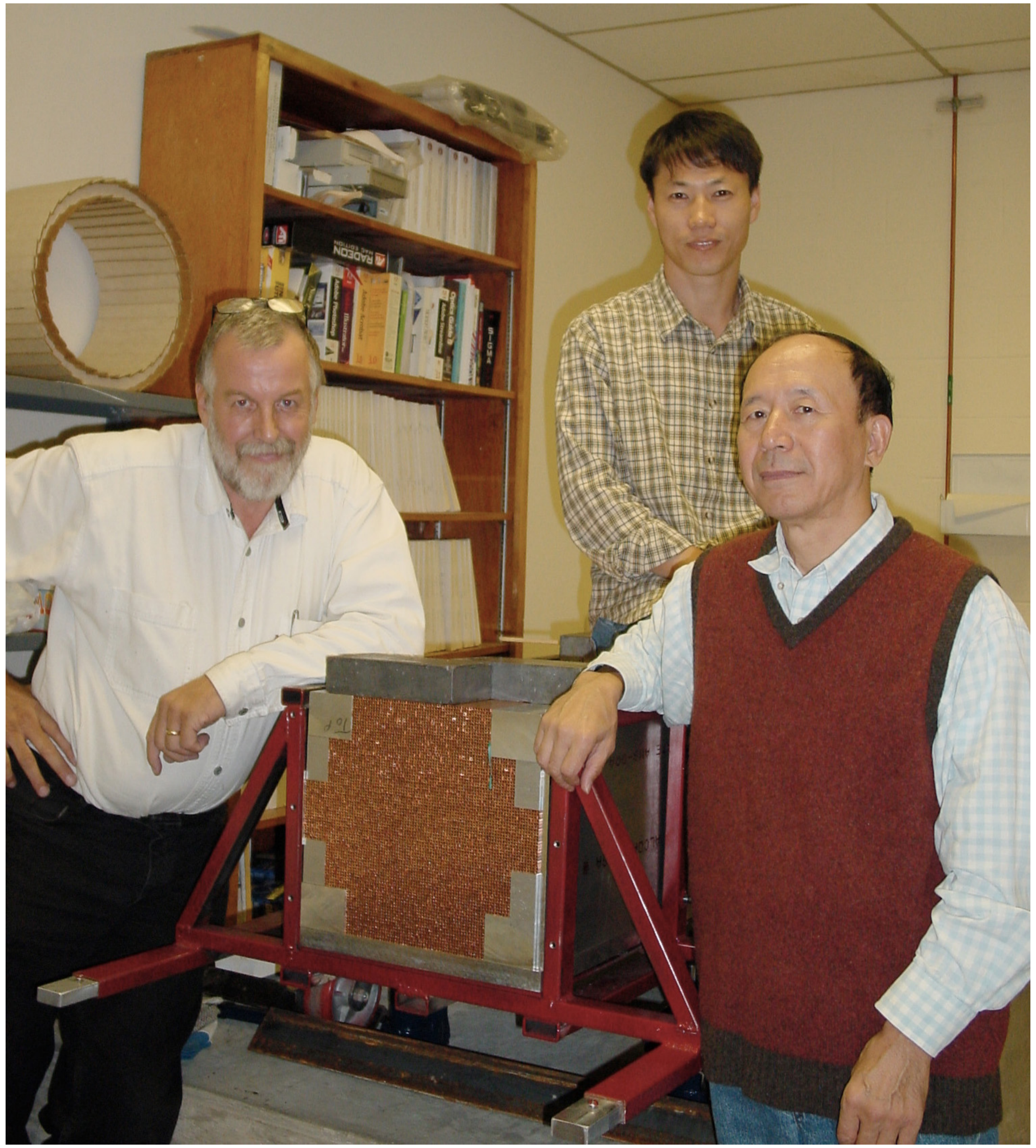

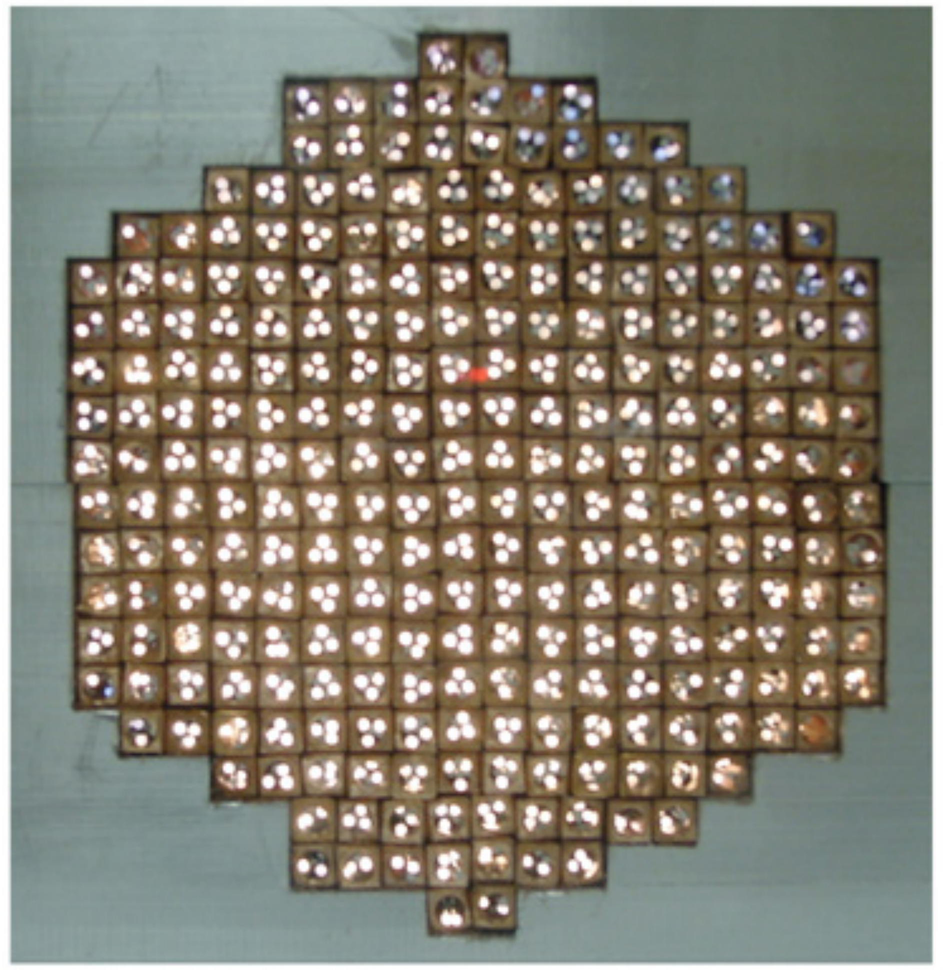

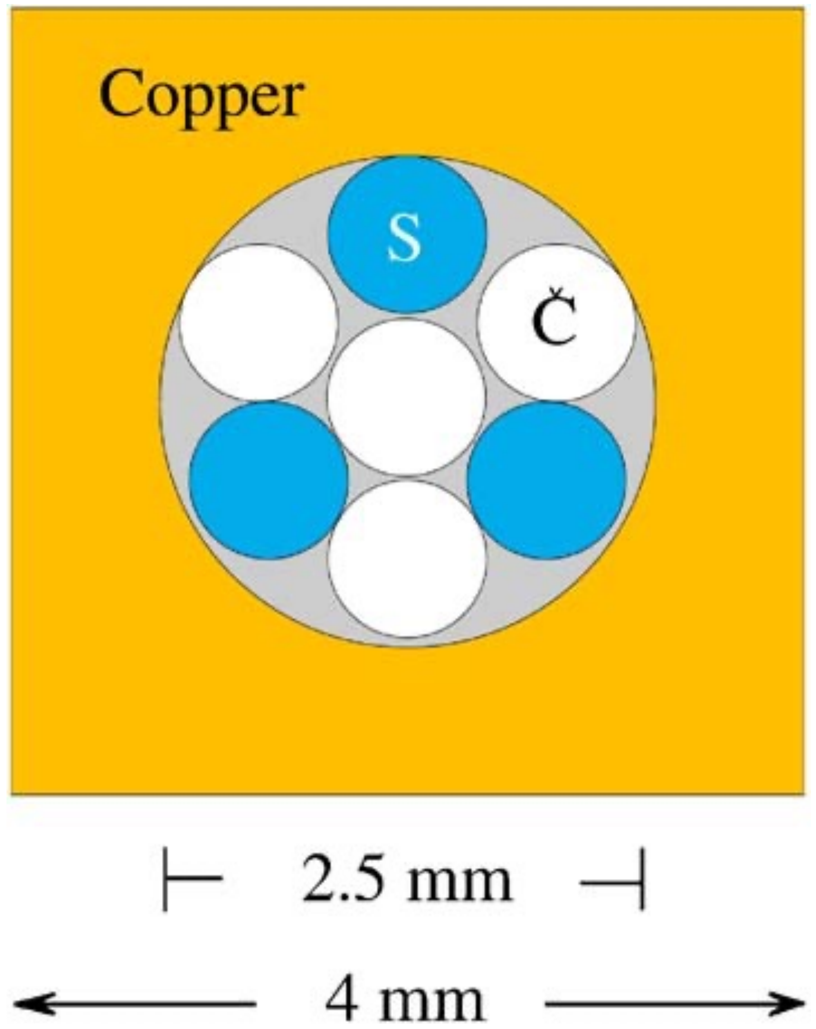

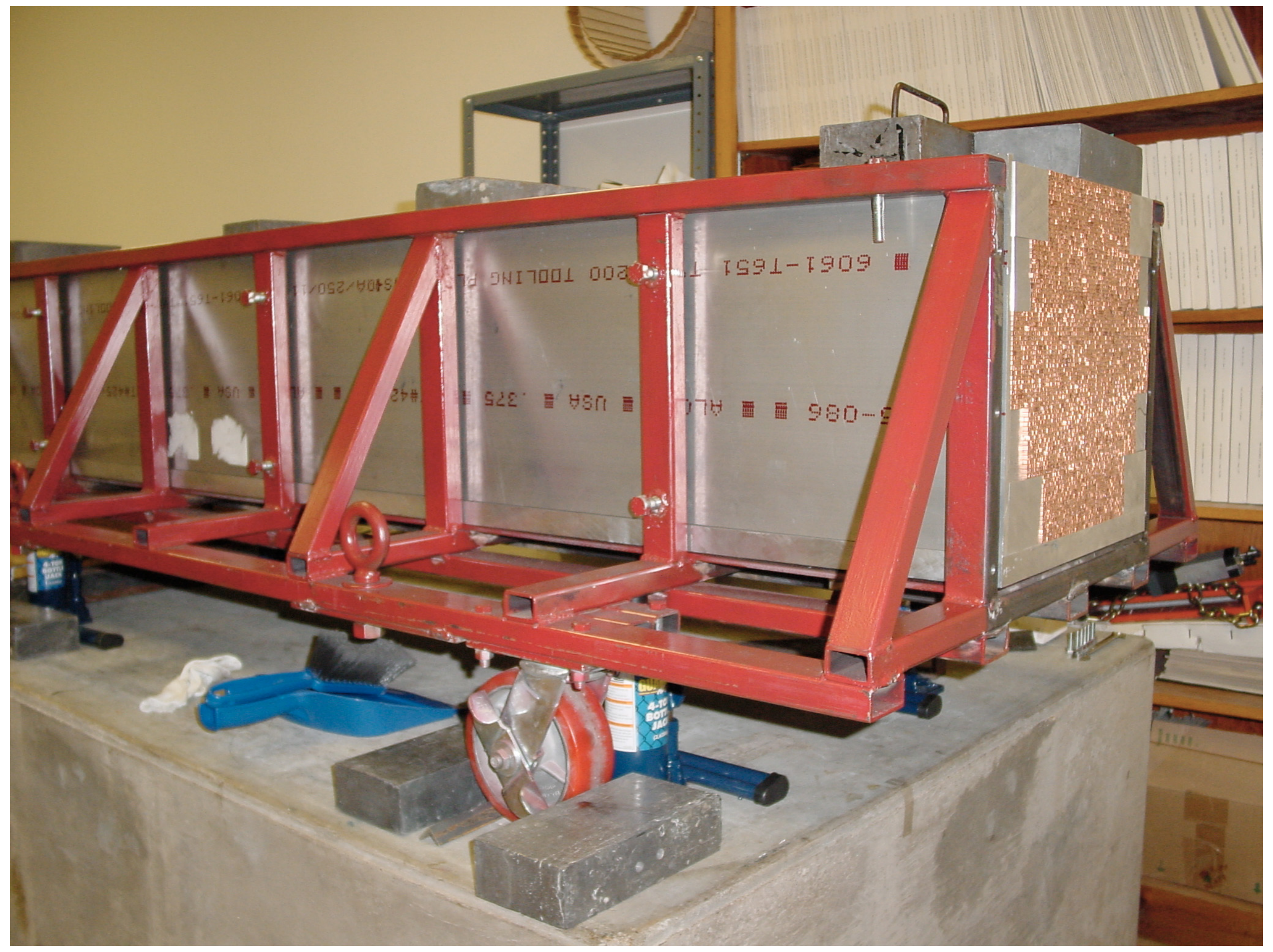

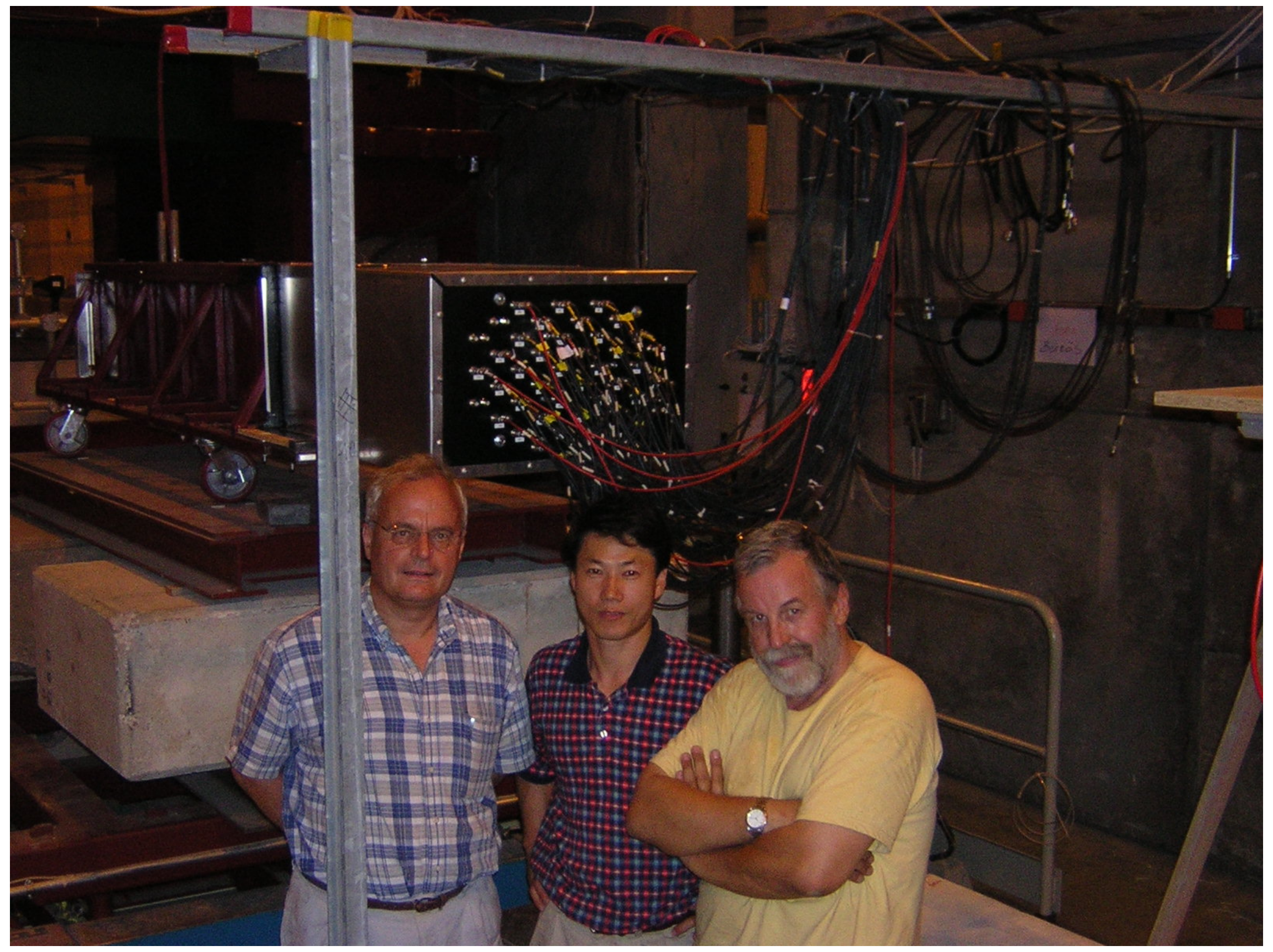

2005

[3] NIM A 533 (2005) 305

- Muon detection with a dual-readout calorimeter

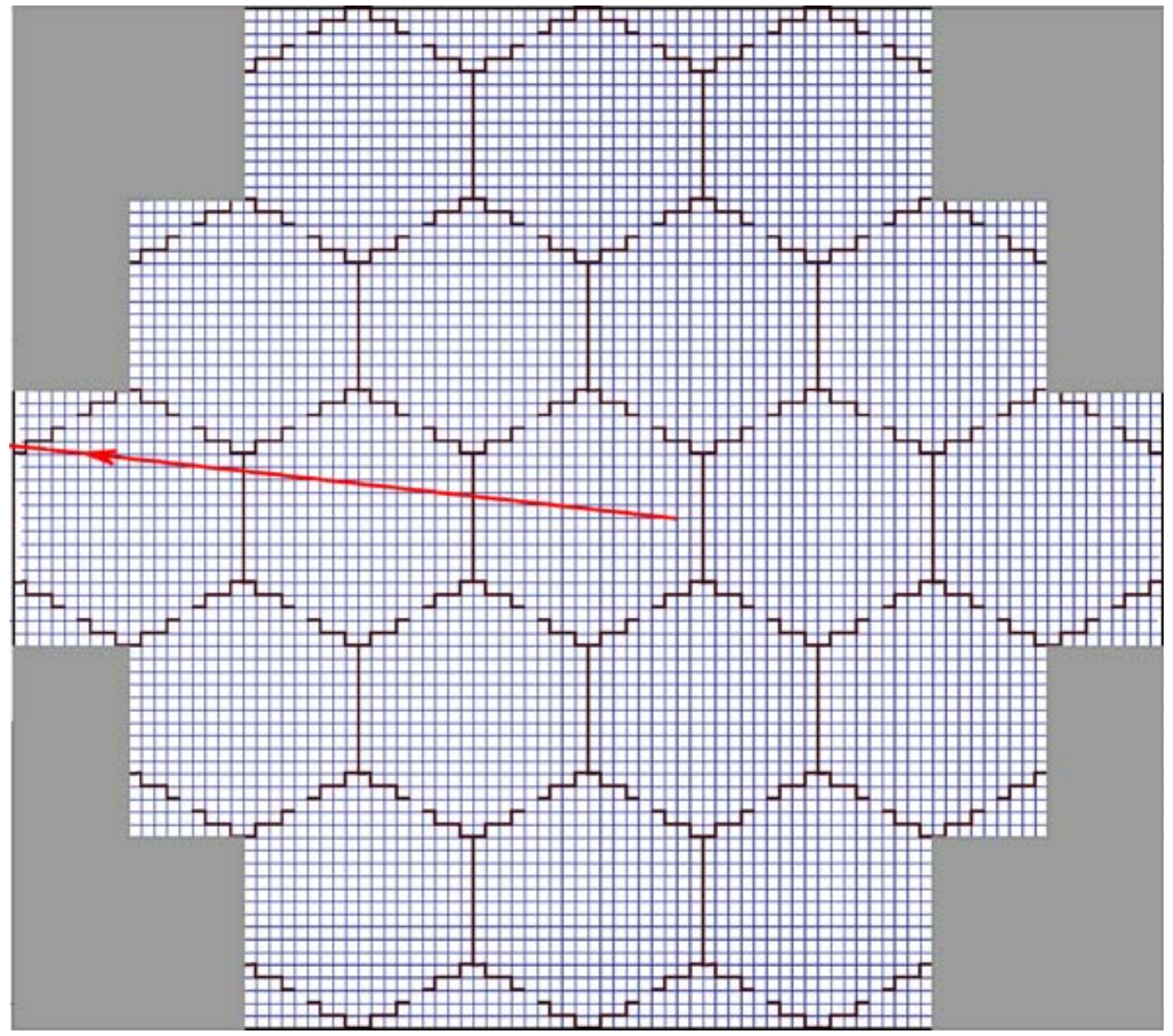

Fig. 2. Layout of the DREAM calorimeter. The detector consists of 19 hexagonal towers. A central tower is surrounded by two hexagonal rings, the Inner Ring (6 towers) and the Outer Ring (12 towers). The towers are not longitudinally segmented. The arrow indicates the (projection of the) trajectory of a muon traversing the calorimeter oriented in position D(6°, 0.7°).

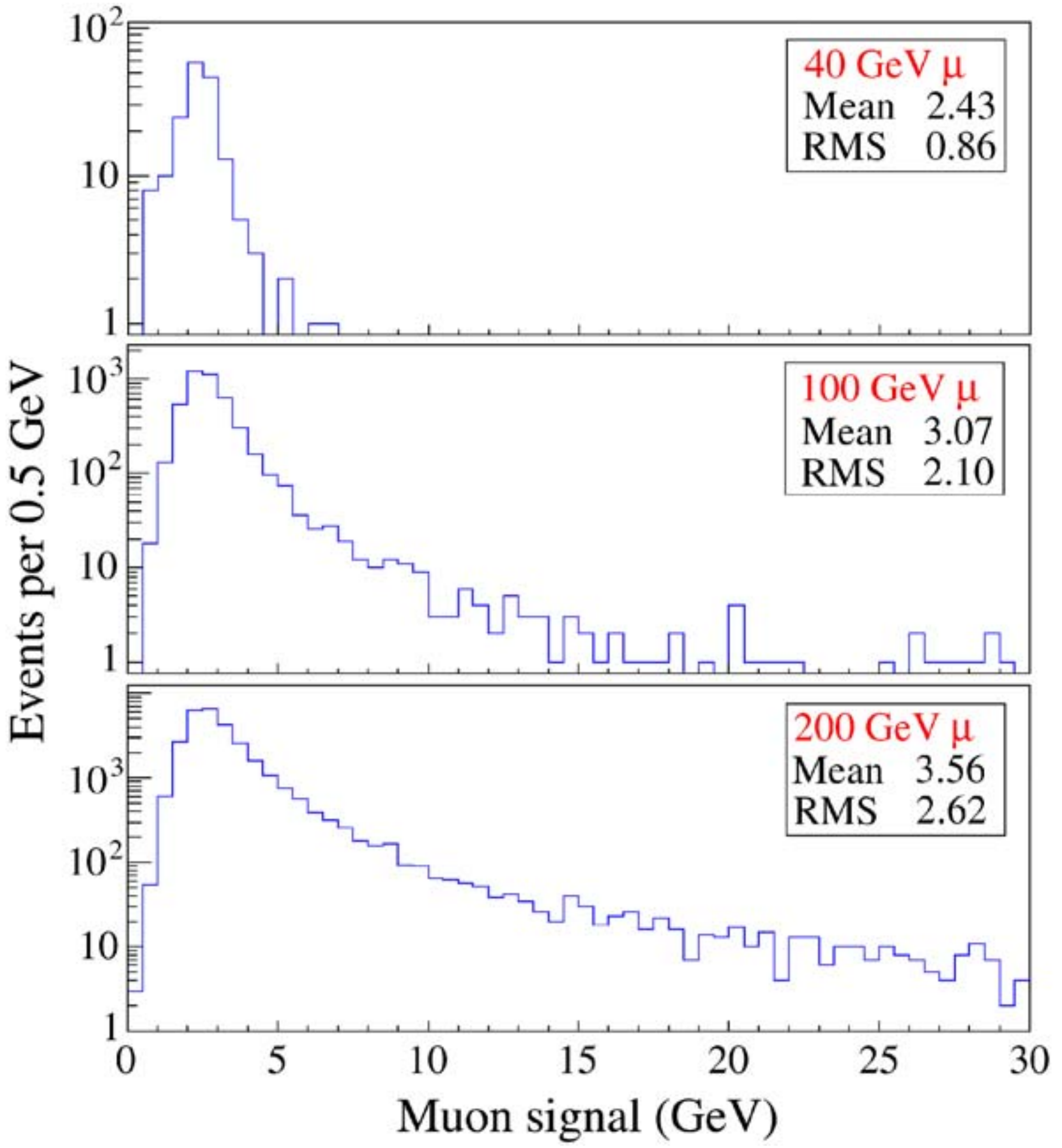

Fig. 14. Signal distributions for 40, 100 and 200 GeV muons, measured with the scintillating fibers in the DREAM calorimeter.

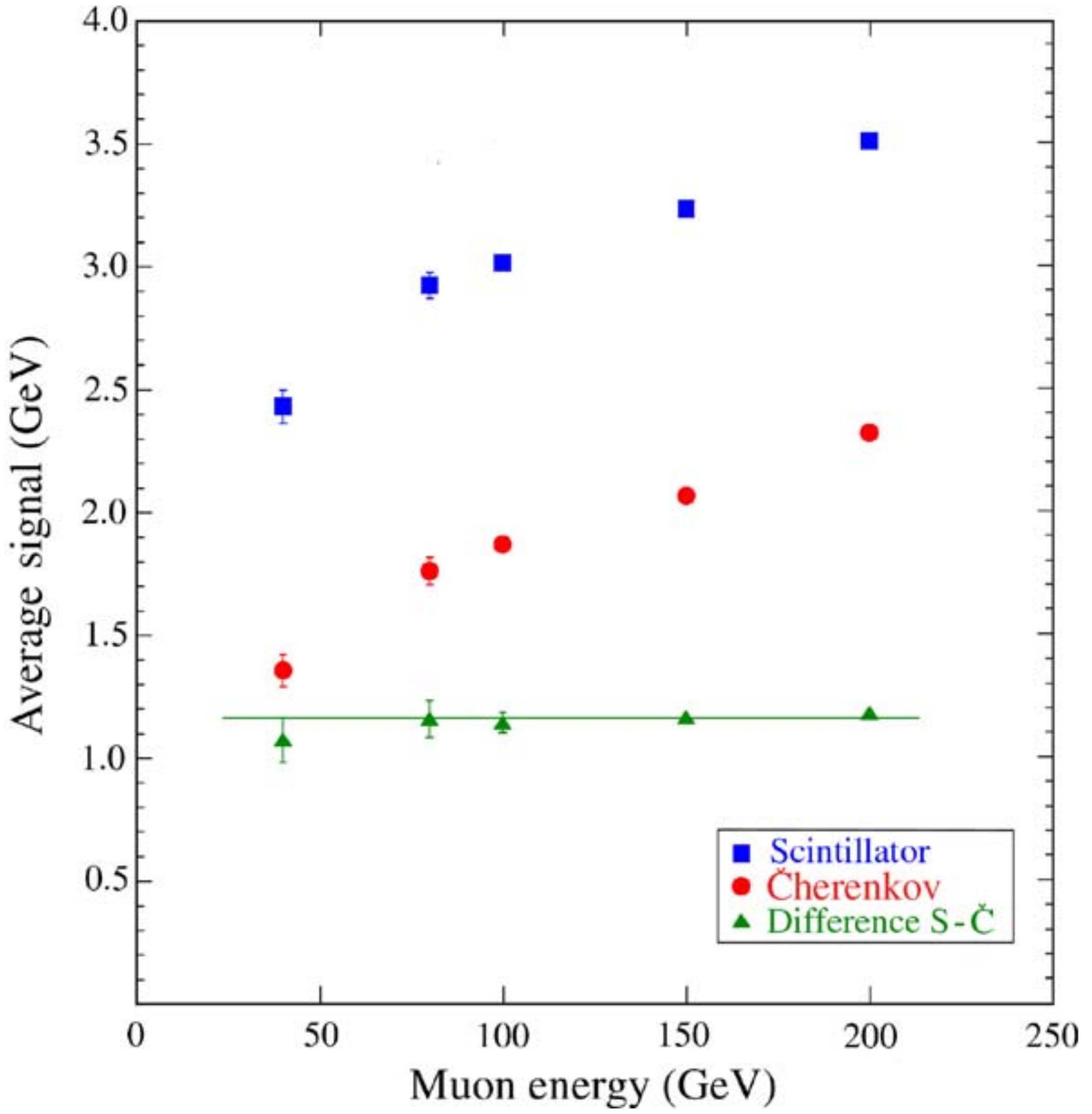

Fig. 18. Average signal from muons traversing the DREAM calorimeter, as a function of the muon energy. The detector was oriented in position D(6°, 0.7°). Results are given separately for the scintillating and the Cherenkov fibers. Also shown is the *difference* between the average signal values from both media.

2005

[4] NIM A 536 (2005) 29

- Electron detection with a dual-readout calorimeter

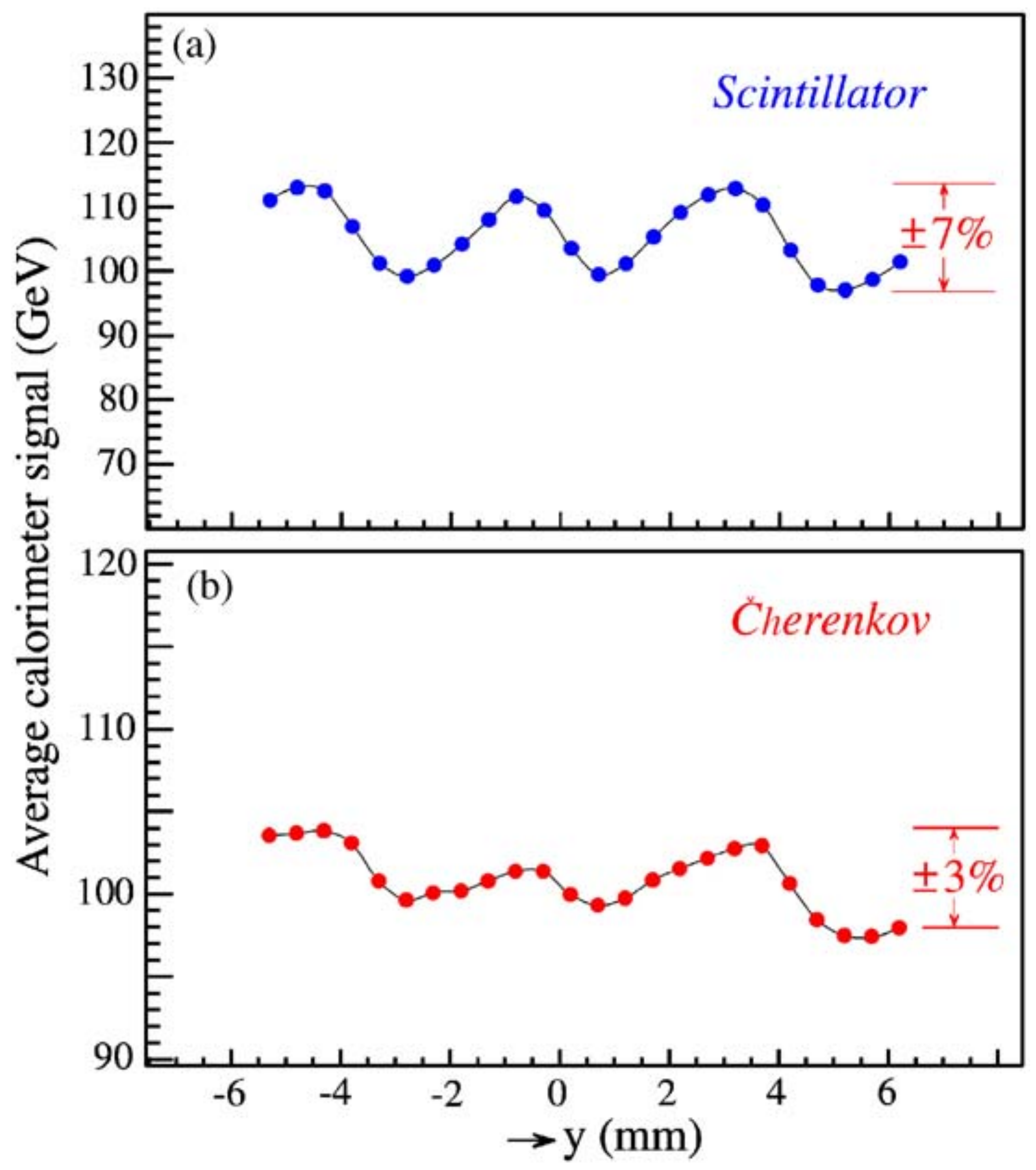

Fig. 11. Average calorimeter signal as a function of the y-coordinate of the impact point, for the scintillator (a) and Cherenkov (b) signals from 100 GeV electrons entering the DREAM calorimeter oriented in the untilted position, A(2°, 0.7°). Note the different vertical scales.

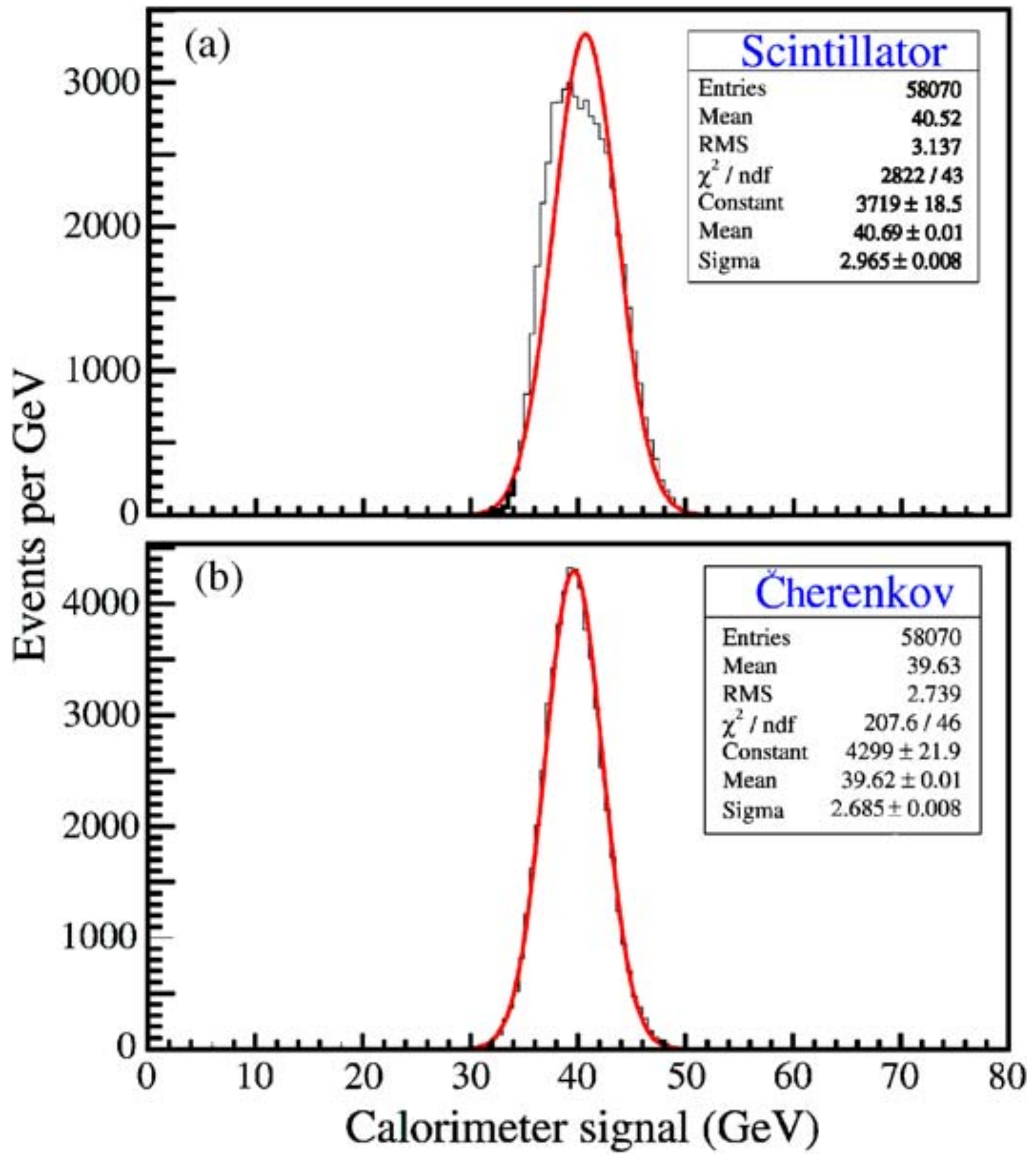

Fig. 7. Signal distributions for 40 GeV electrons, recorded from the scintillating (a) and the Cherenkov (b) fibers, with the DREAM calorimeter in the untilted position, A(2°, 0.7°).

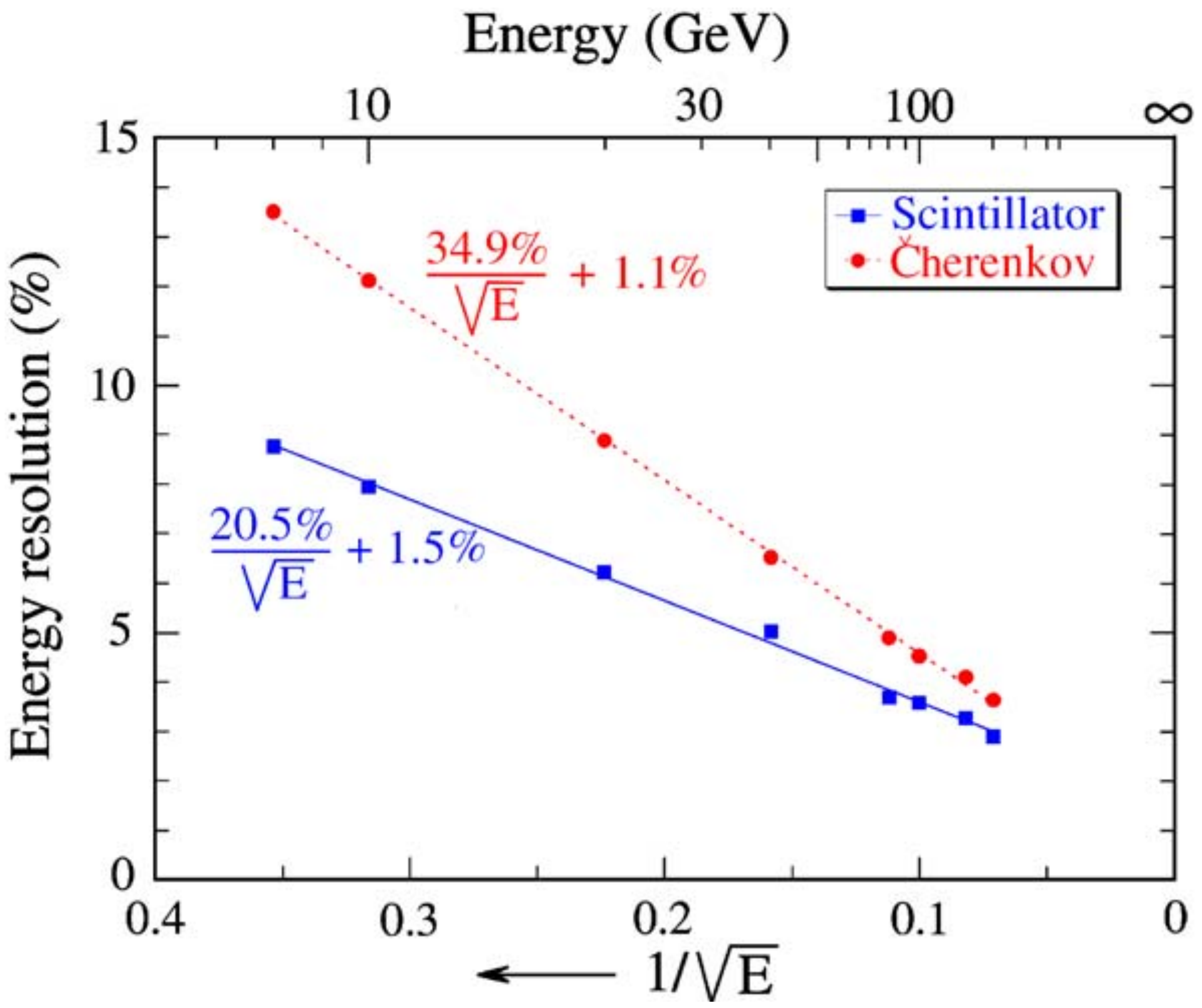

Fig. 20. The energy resolution as a function of energy, measured with the scintillating (squares) and Cherenkov fibers (circles), for electrons entering the calorimeter in the tilted position, B(3°, 2°).

2005

[5] NIM A 537 (2005) 537

- Hadron and jet detection with a dual-readout calorimeter

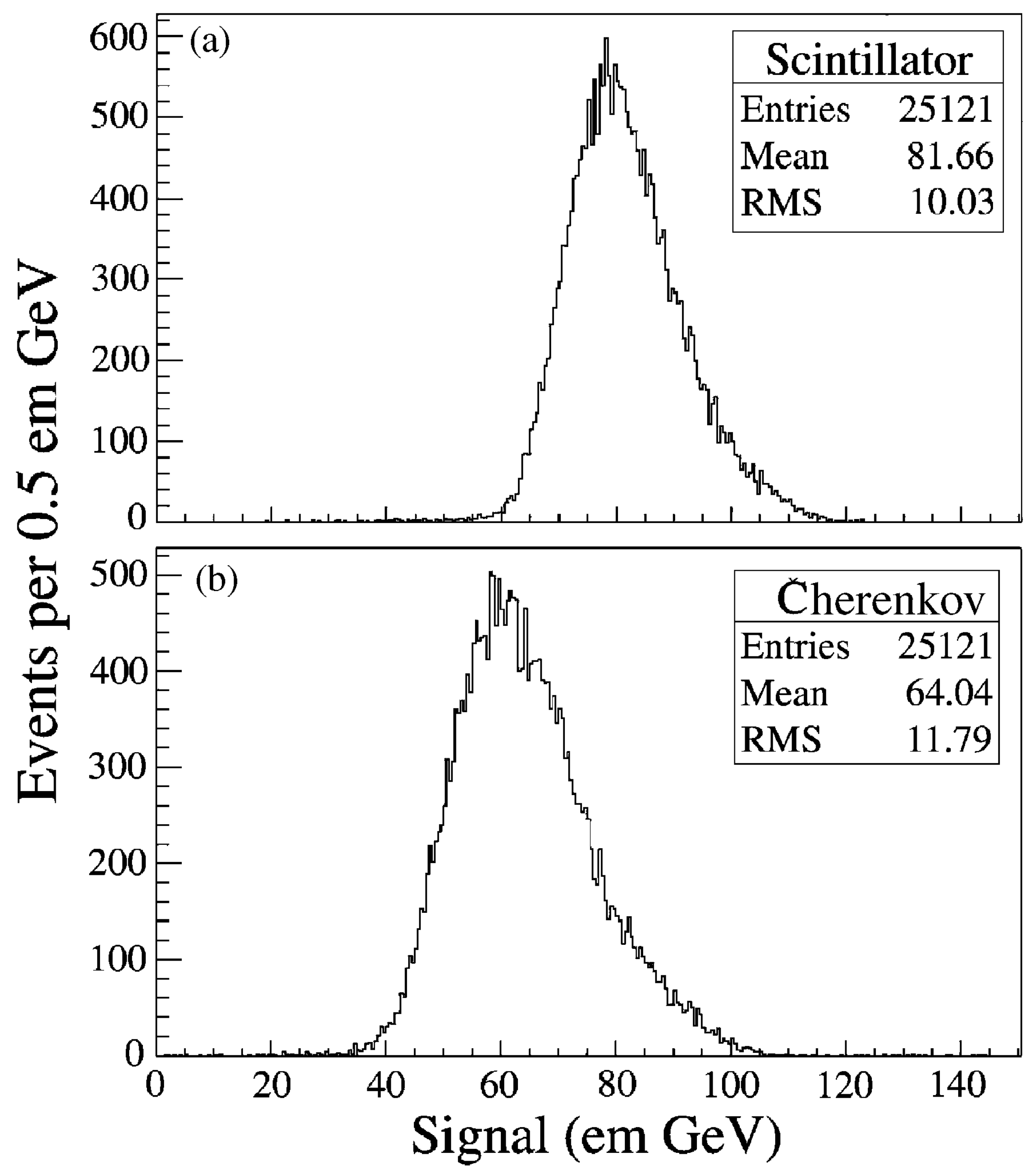

Fig. 9. Signal distributions for 100 GeV π^- recorded by the scintillating (a) and Cherenkov (b) fibers of the DREAM calorimeter, oriented in the untilted position, $A(2°, 0.7°)$. The signals are expressed in the same units as those for em showers, which were used to calibrate the detector (em GeV).

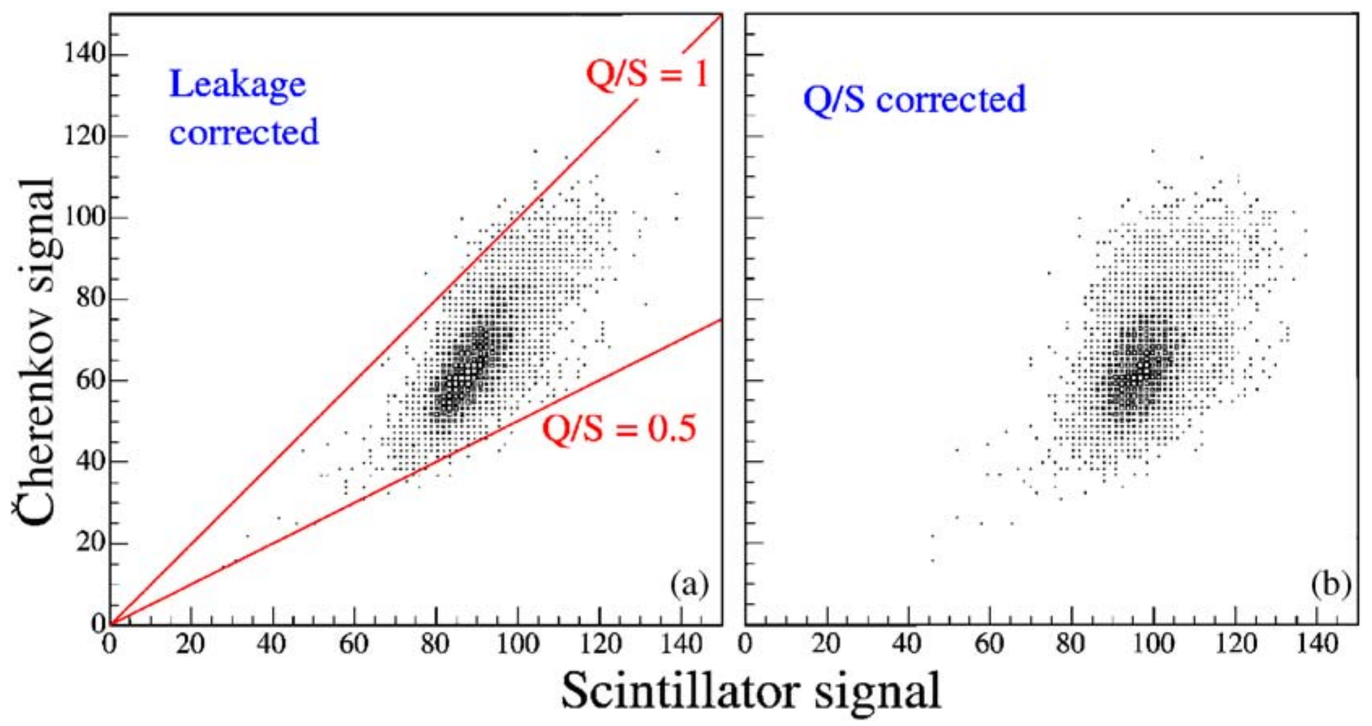

Fig. 24. Cherenkov signals versus scintillator signals for 100 GeV π^- in the DREAM calorimeter. These plots were derived from the raw data (Fig. 12) after applying corrections for shower leakage, using Eq. (6) (a) and, in addition, for the effects of non-compensation, using Eq. (7) (b).

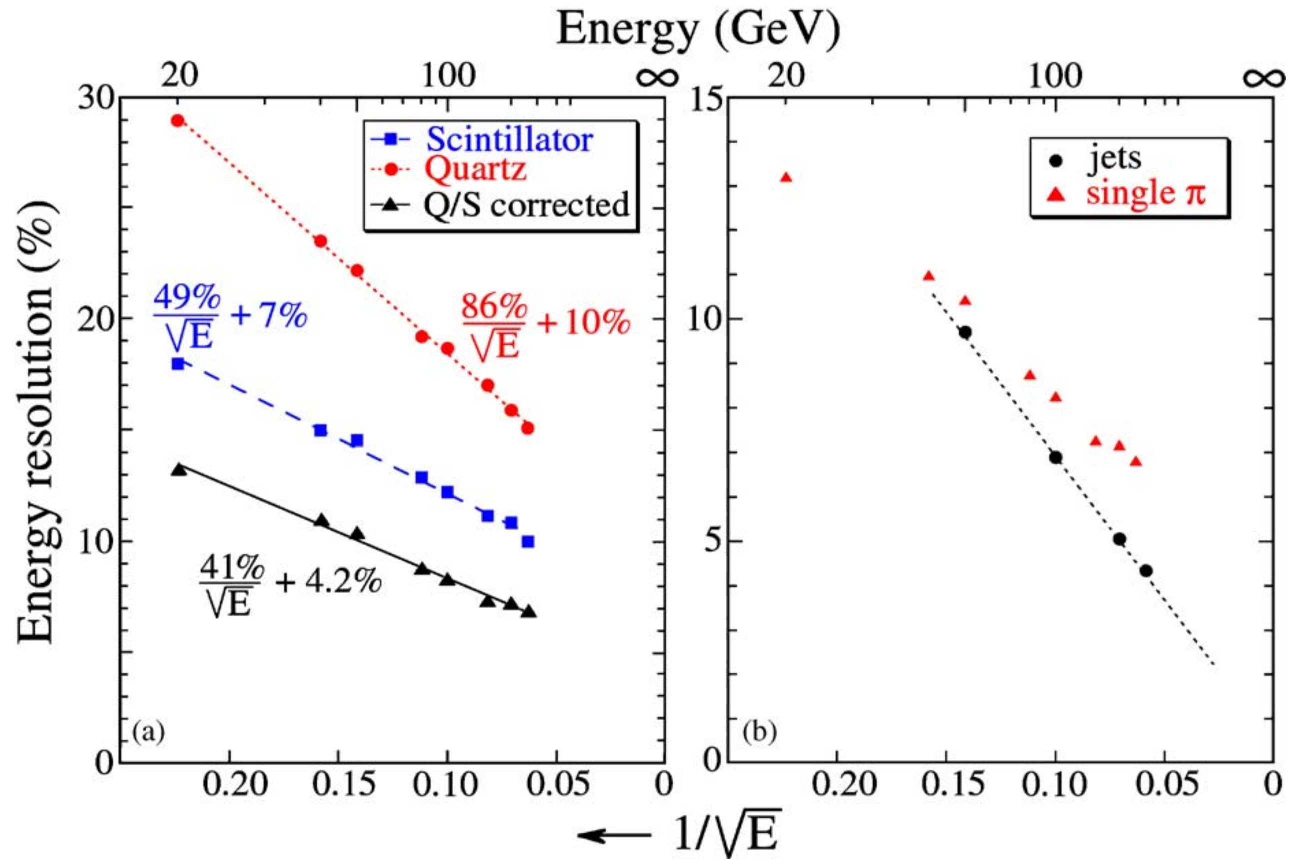

Fig. 32. The energy resolution for single pions as a function of energy, measured with the scintillation fibers and the Cherenkov fibers, and after corrections made on the basis of the measured Q/S signal ratio (a). Comparison of the corrected resolutions for jets and single pions (b).

2009

[16] NIM A 598 (2009) 710

- Neutron Signals for Dual-Readout Calorimetry

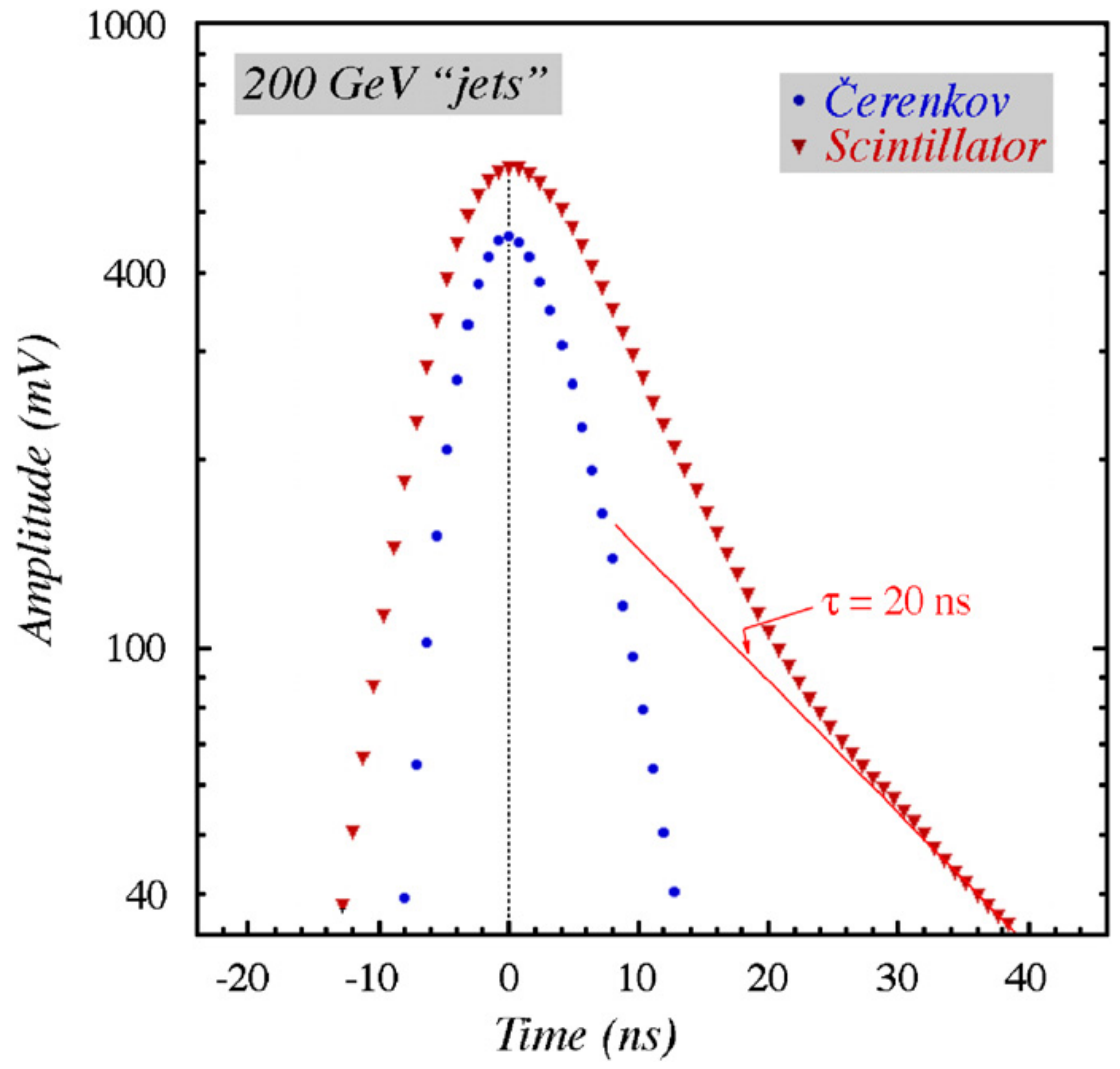

Fig. 4. Average time structure of the Cherenkov and scintillation signals recorded for 200 GeV "jets" developing in the DREAM calorimeter. The scintillation signals exhibit a tail with a time constant of about 20 ns, which is absent in the Cherenkov signals.

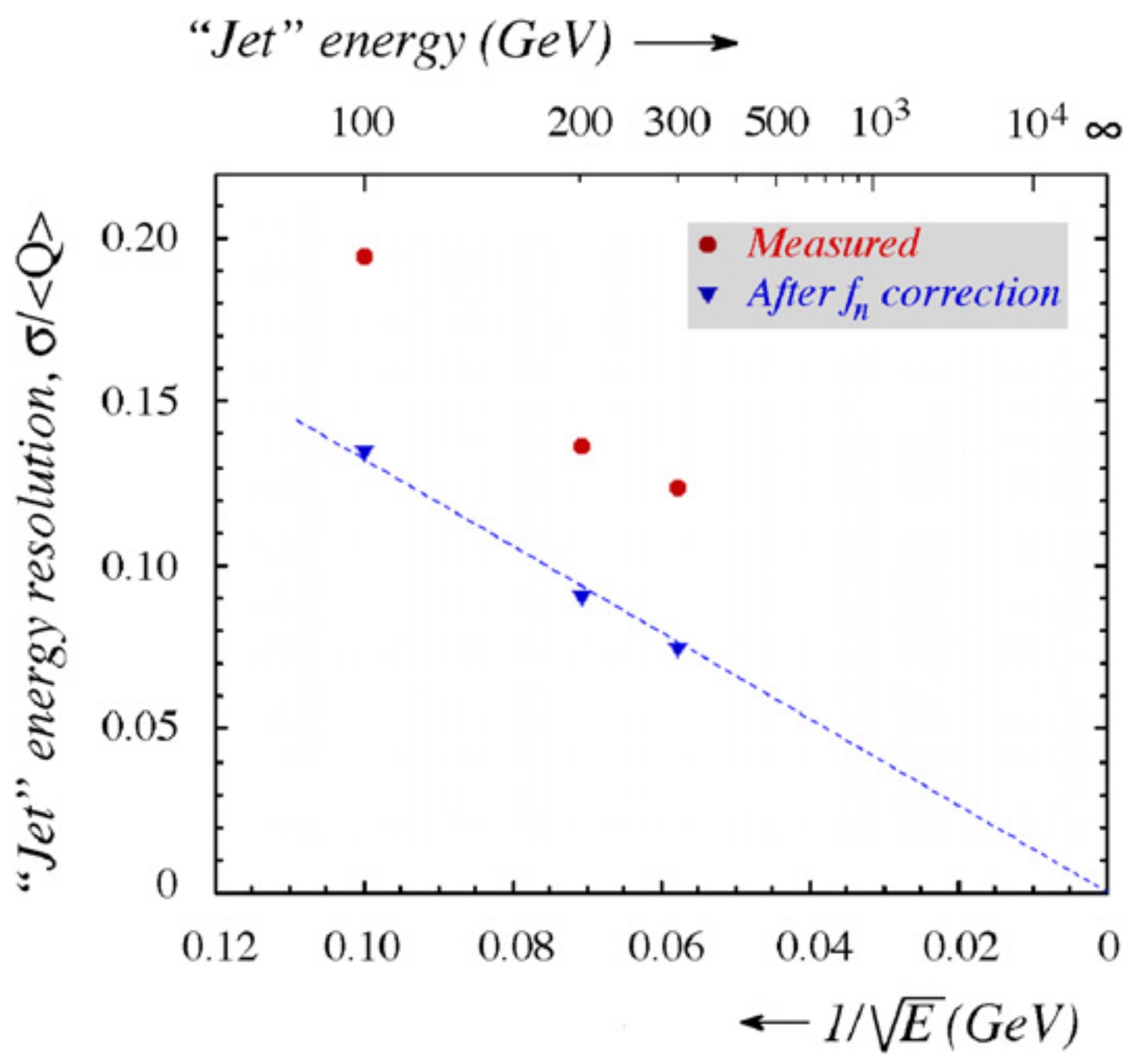

Fig. 11. Relative width of the Cherenkov signal distribution for "jets" as a function of energy, before and after a correction that was applied on the basis of the relative contribution of neutrons to the scintillator signals.

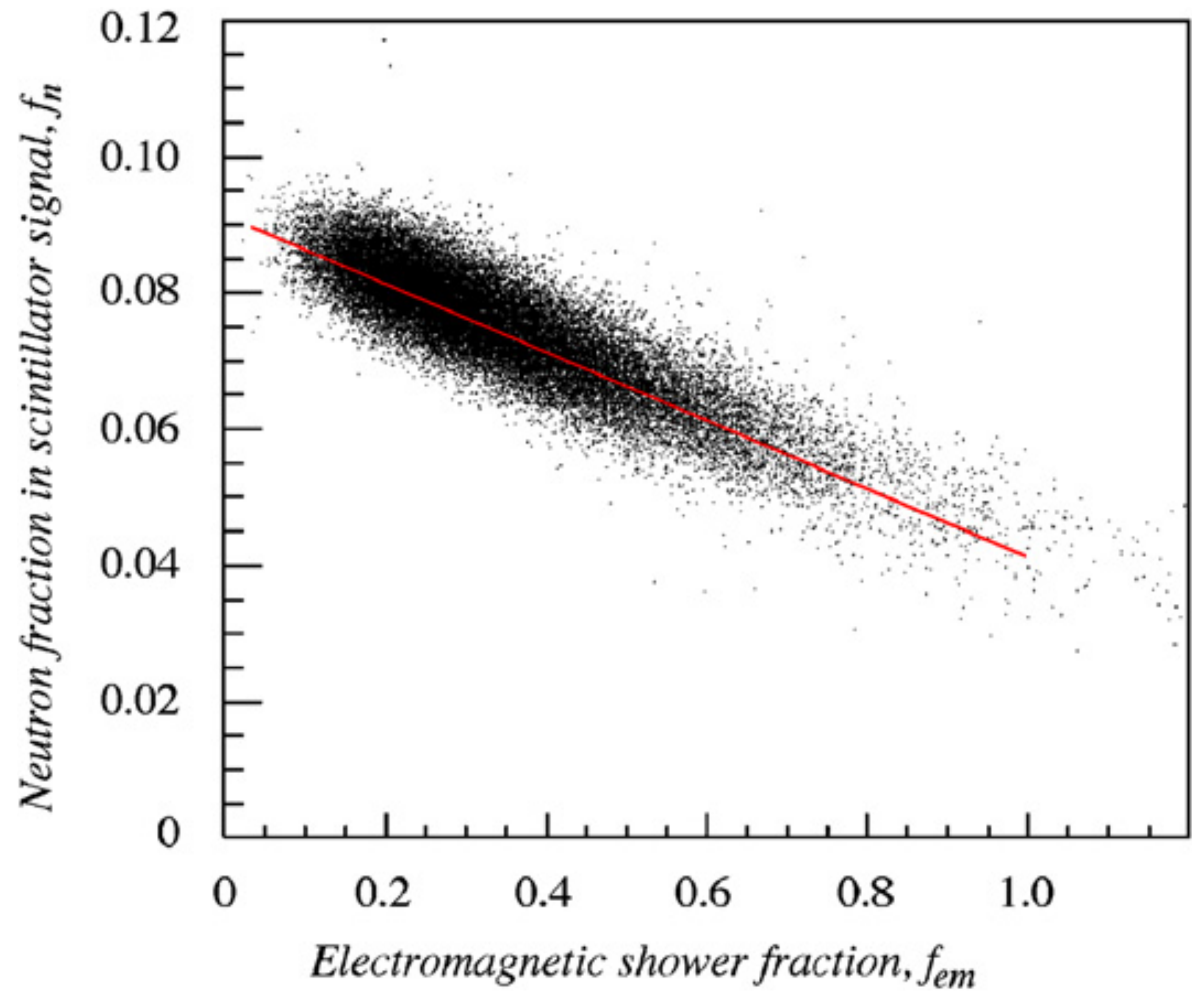

Fig. 12. Relationship between the average fractional contribution of neutrons to the scintillator signals and the em fraction of the showers induced by 200 GeV "jets".

2009

[19] NIM A 610 (2009) 488

- Dual-readout calorimetry with a full-size BGO electromagnetic section

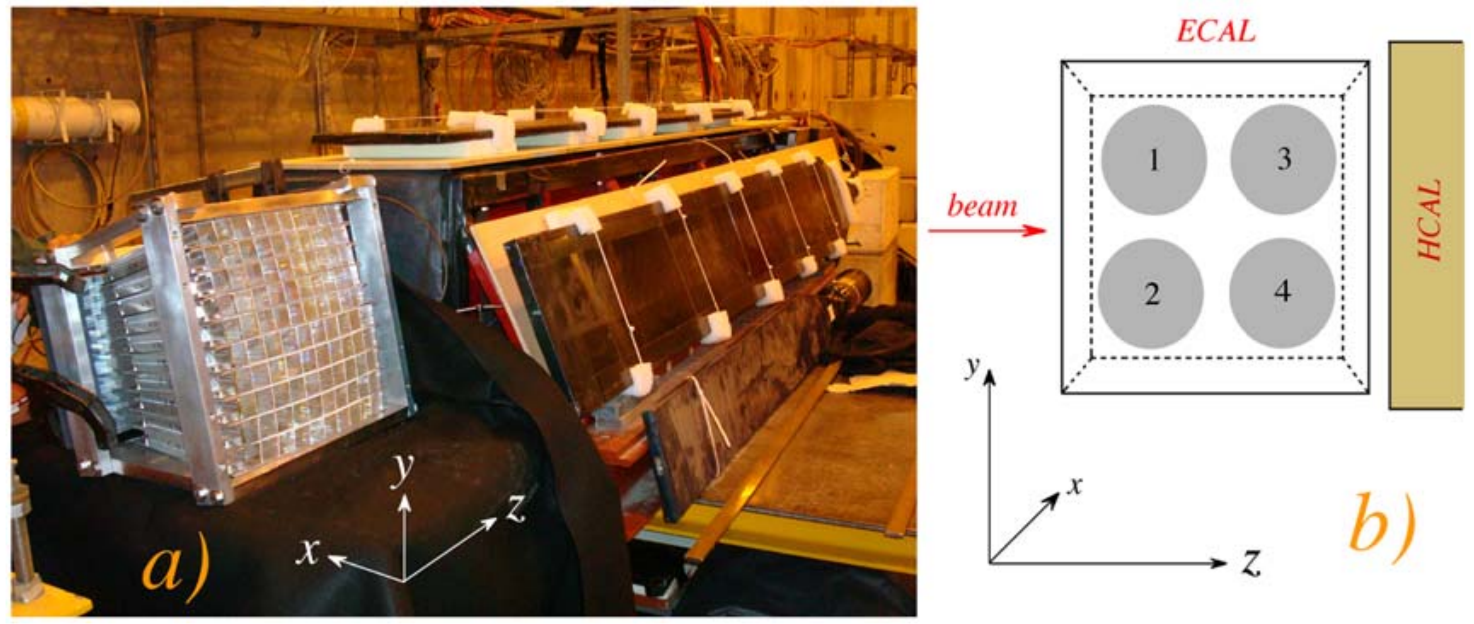

Fig. 1. The calorimeter during installation in the H4 test beam, which runs from the bottom left corner to the top right corner in this picture. The 100-crystal BGO matrix is located upstream of the fiber calorimeter, and is read out by four PMTs on the left (small end face) side. Some of the leakage counters are visible as well (a). The location and numbering of the PMTs reading out the BGO crystal matrix (b).

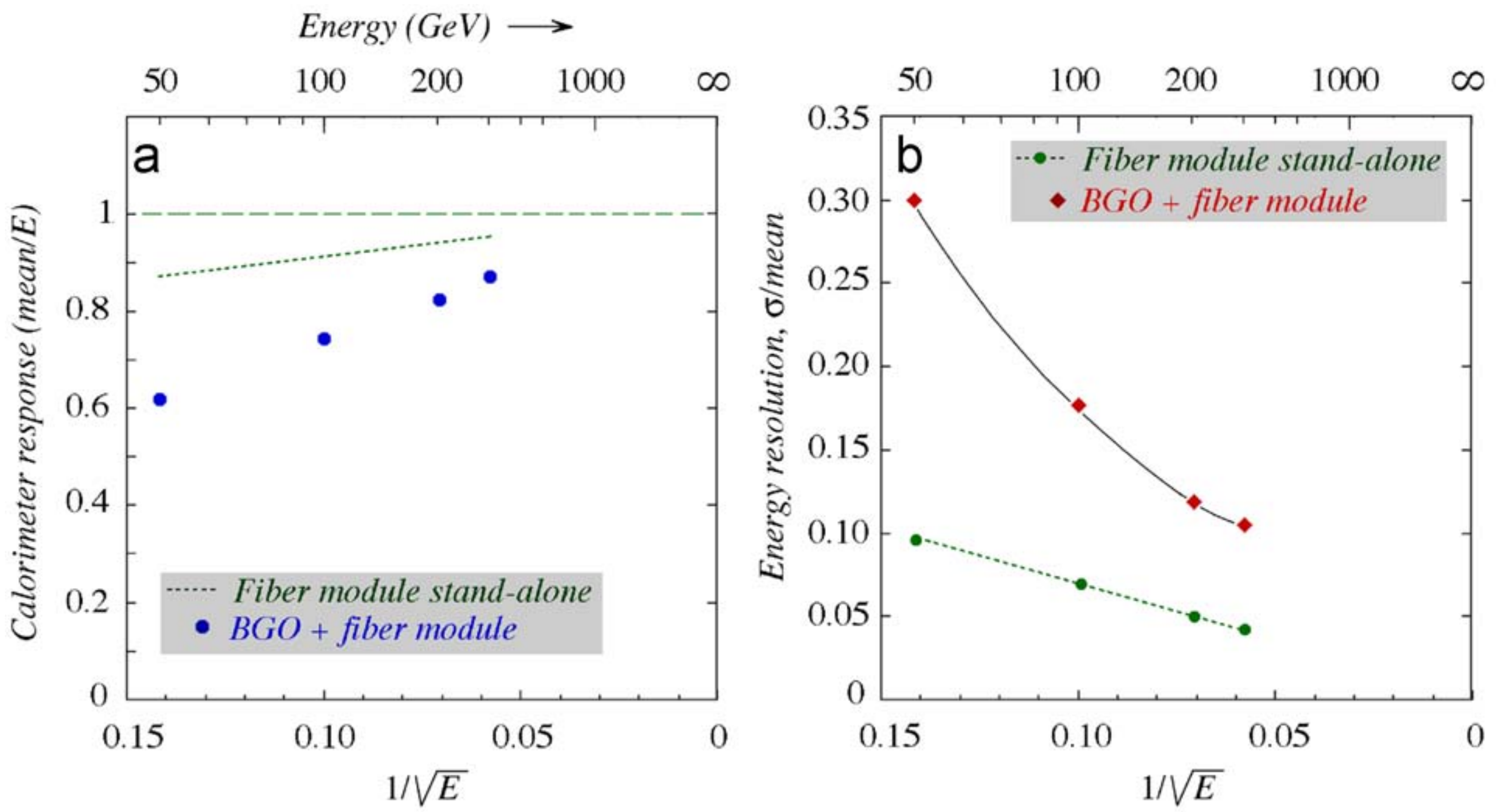

Fig. 18. The calorimeter response (a) and the energy resolution (b) for "jet" events detected in the BGO + fiber calorimeter system, corrected for the effects of fluctuations in f_{em} by means of Eq. (4) (using $\xi_{eff} = 0.4$), as function of the "jet" energy. The results obtained previously for the fiber calorimeter module in stand-alone mode [4] are indicated by dotted lines.

What we learned with the prototype DREAM calorimeter

- Reduction of shower leakage (leakage fluctuations)→Build larger detector
- Increase Cerenkov light yield
  - Prototype DREAM: 8 p.e./GeV → light yield fluctuations contribute by 35%/ $\sqrt{E}$
- Reduction of sampling fluctuations
  - contribute ~40%/$\sqrt{E}$ to hadronic resolution (single pions)

RD52 Cu- and Pb-fiber Calorimeters

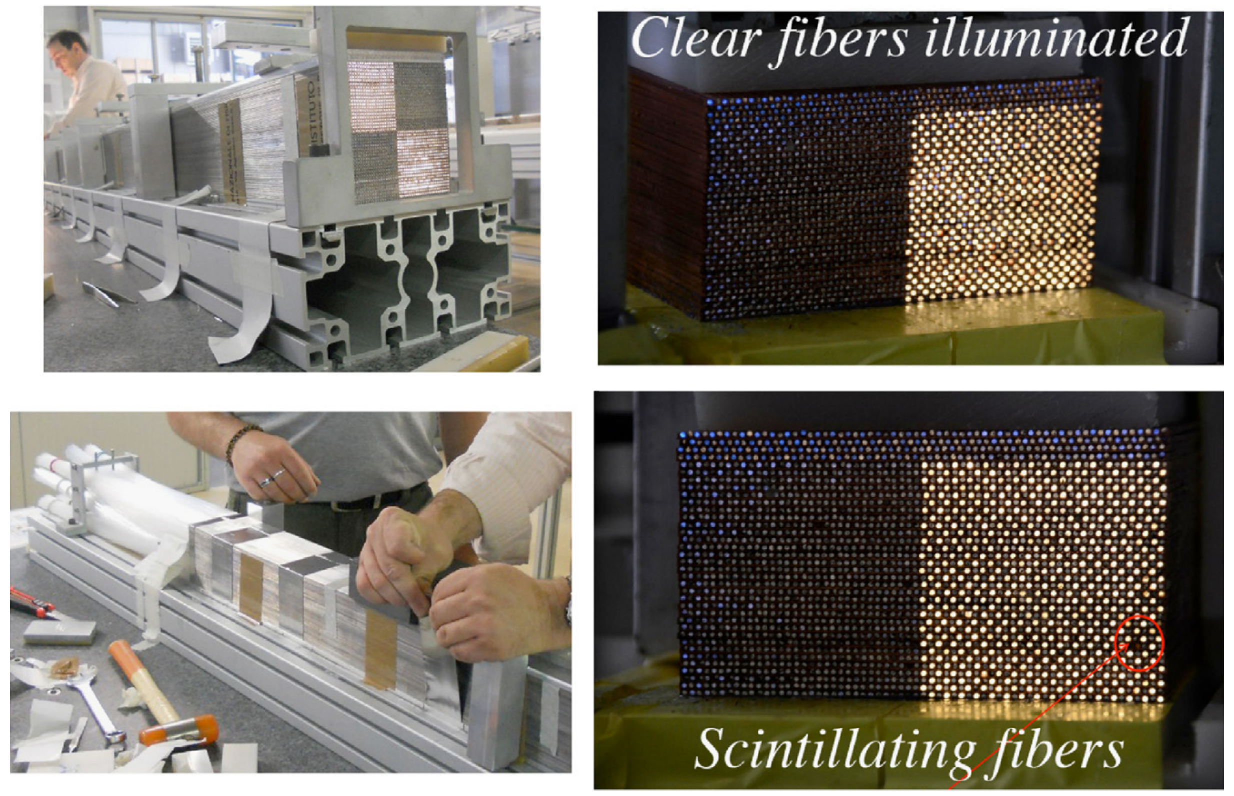

Fig. 2. Pictures of the first SuperDREAM modules built with lead (*left*) or copper (*right*) as absorber material. The alternating arrangement of clear and scintillating fibers in each row of the copper modules is illustrated by illuminating the fiber bunches from the rear end.

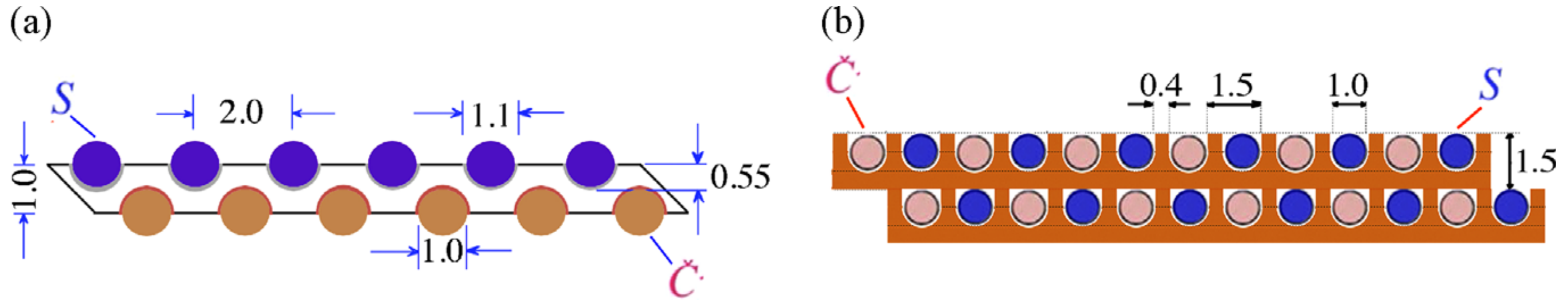

Fig. 3. Basic structure of the new lead (a) and copper (b) based RD52 fiber calorimeters.

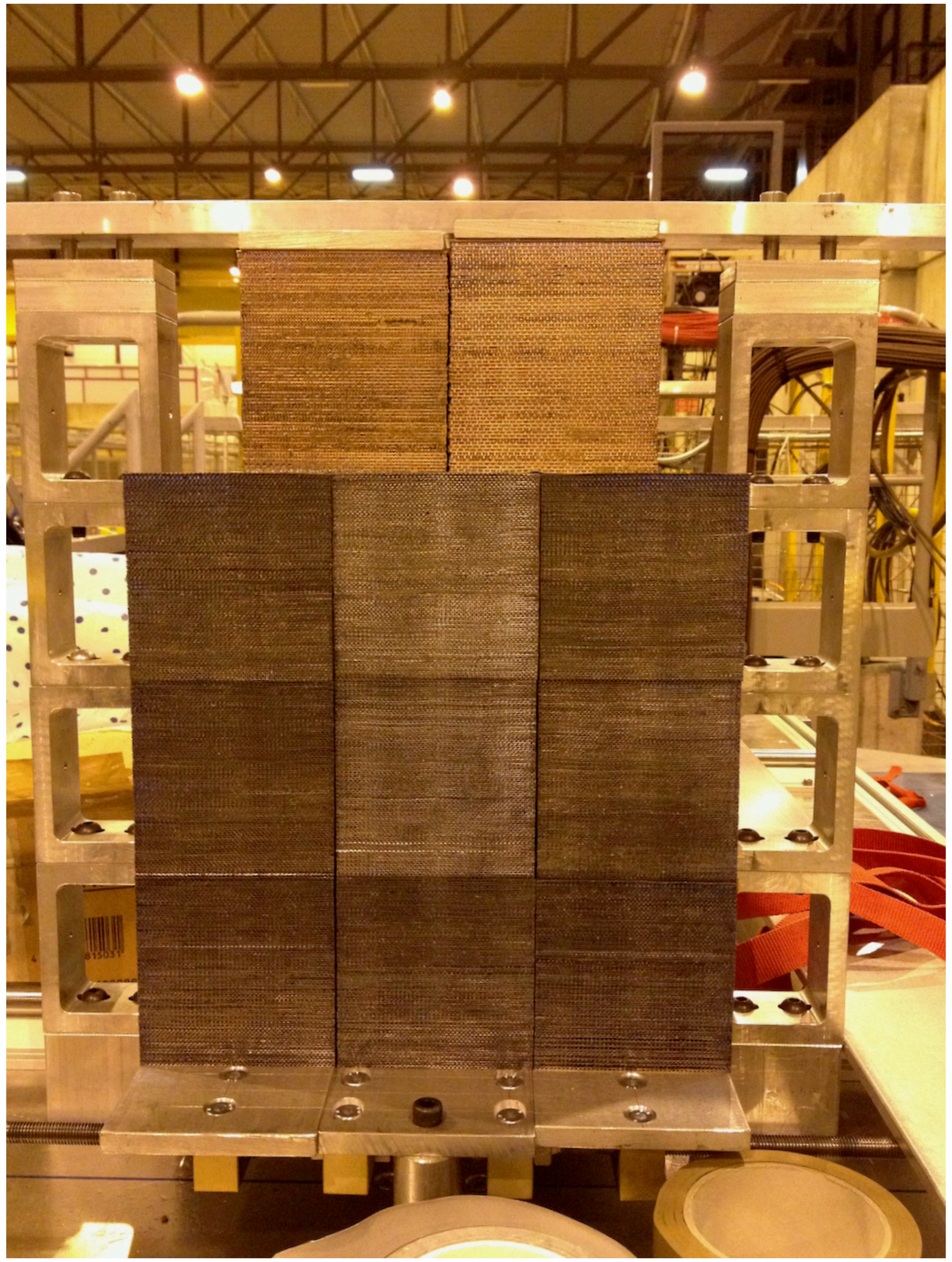

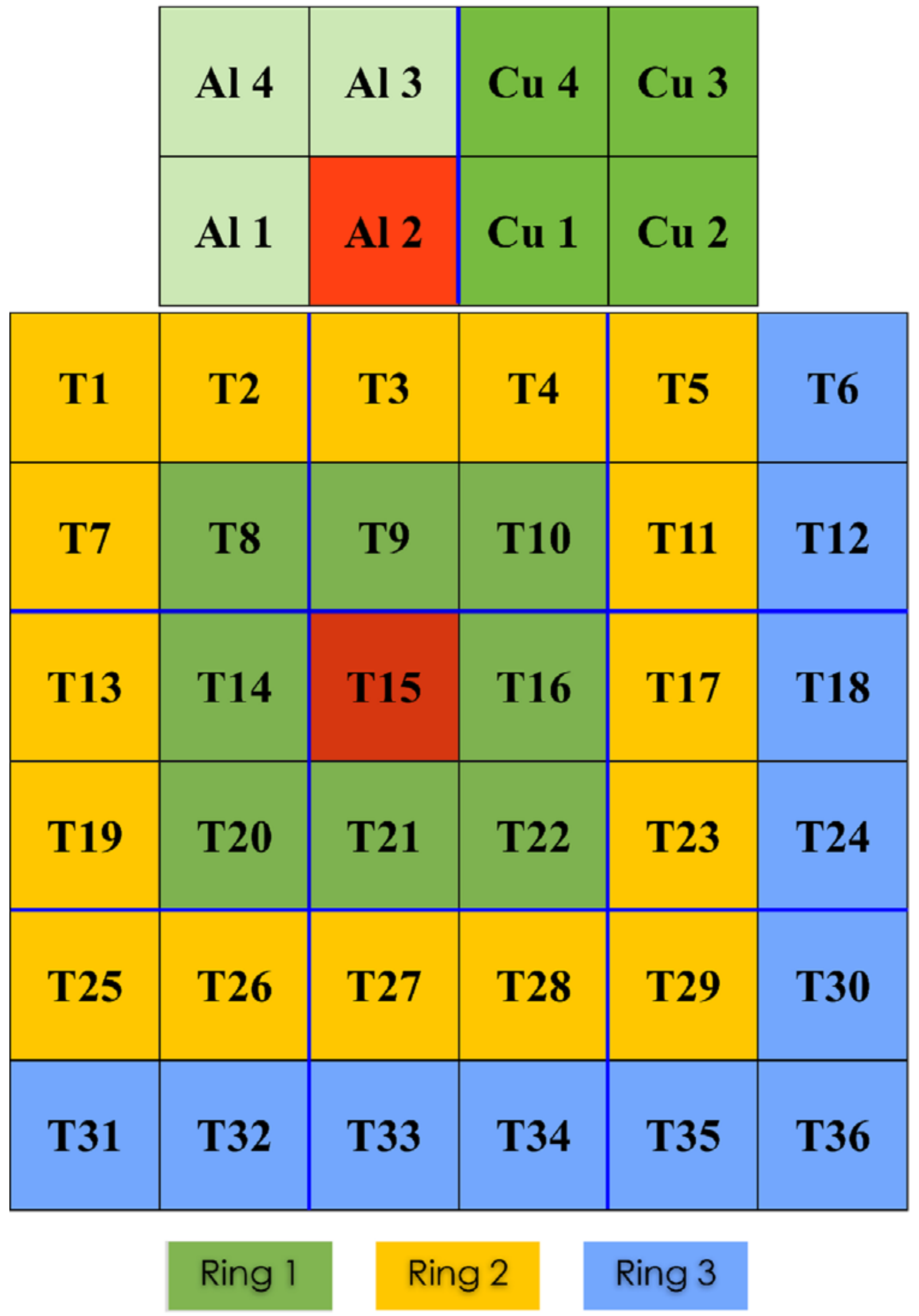

Fig. 4. The RD52 SuperDREAM calorimeter as tested at the end of 2012. It consisted of 9 lead-based modules, each consisting of 4 towers (towers 1–36), and two copper-based modules, placed on top of the lead array. The left copper module (of which the towers are marked as “Al”) is equipped with Cherenkov fibers with an aluminized upstream end face. For readout purposes, the lead calorimeter consists of a central tower (T15), surrounded by 3 square rings of towers.

2014

[26] NIM A 735 (2014) 130

- The electromagnetic performance of the RD52 fiber calorimeter

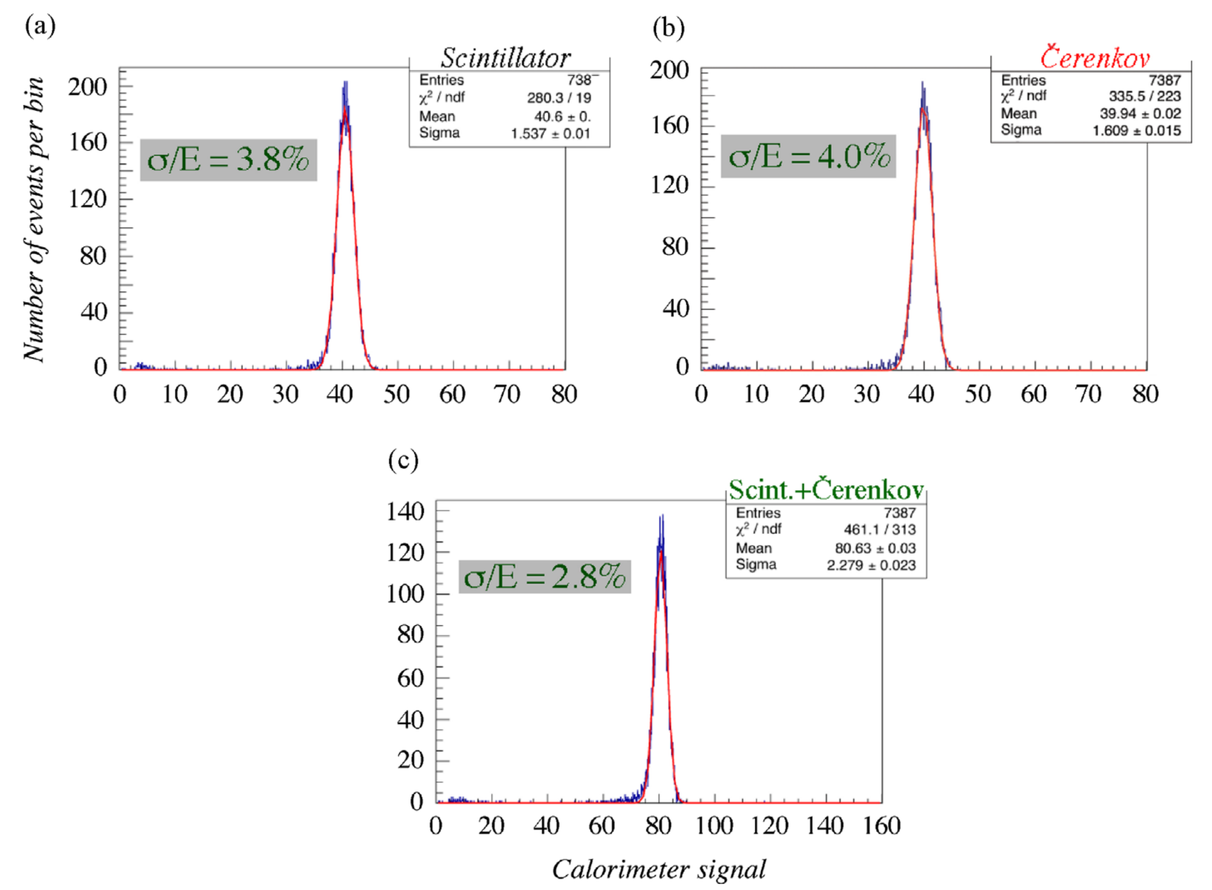

Fig. 8. Signal distributions for 40 GeV electrons in the copper-fiber calorimeter. Shown are the distributions measured with the scintillating fibers (a), the Cherenkov fibres (b) and the sum of all fibers (c). The angle of incidence of the beam particles (θ, ϕ) was (1.5°, 1.0°). The size of the beam spot was 10 × 10 mm^2.

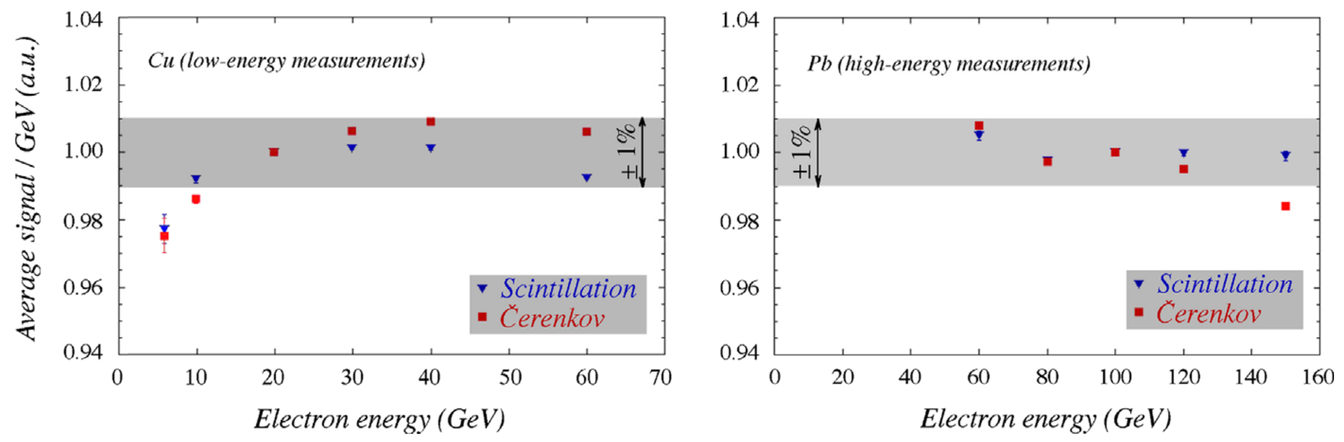

Fig. 9. The linearity of the copper (a) and lead (b) based fiber calorimeters for em shower detection in the scintillation and Cherenkov channels. See text for details.

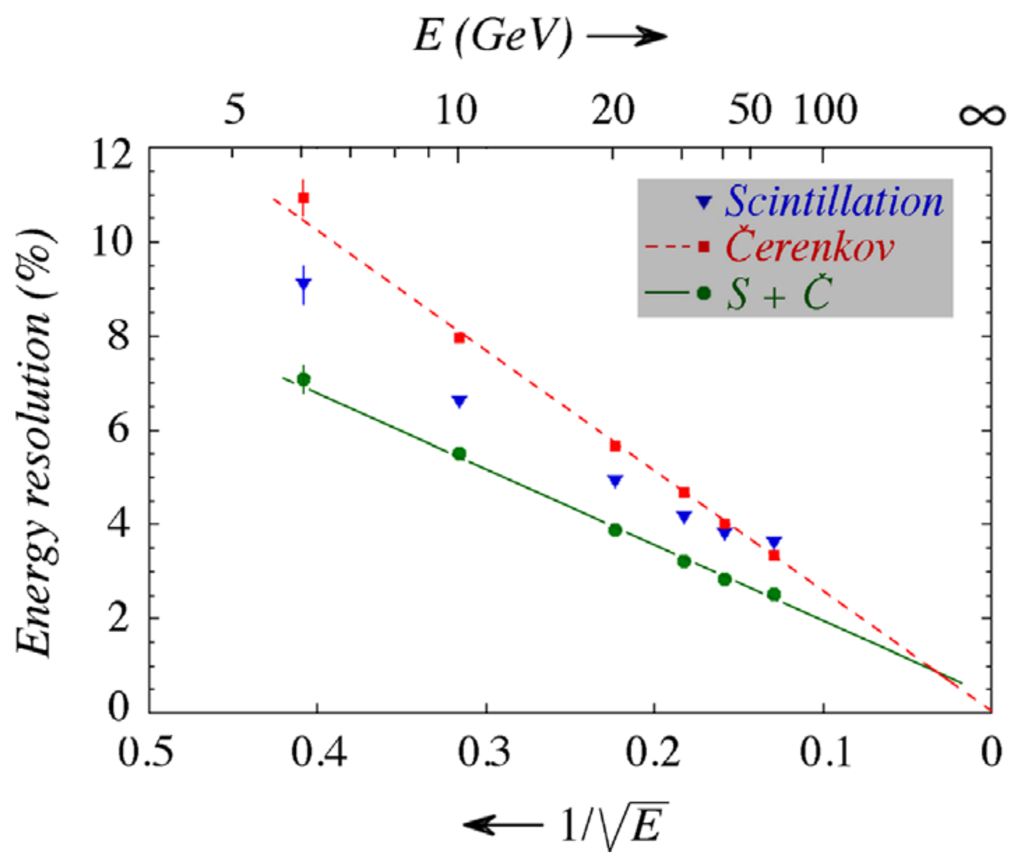

Fig. 13. The energy resolution for electrons in the copper-fiber module, as a function of the beam energy. Shown are the results for the two types of fibers, and for the combined signals. The angle of incidence of the beam particles (θ, ϕ) was (1.5°, 1.0°). The size of the beam spot was 10 × 10 mm^2.

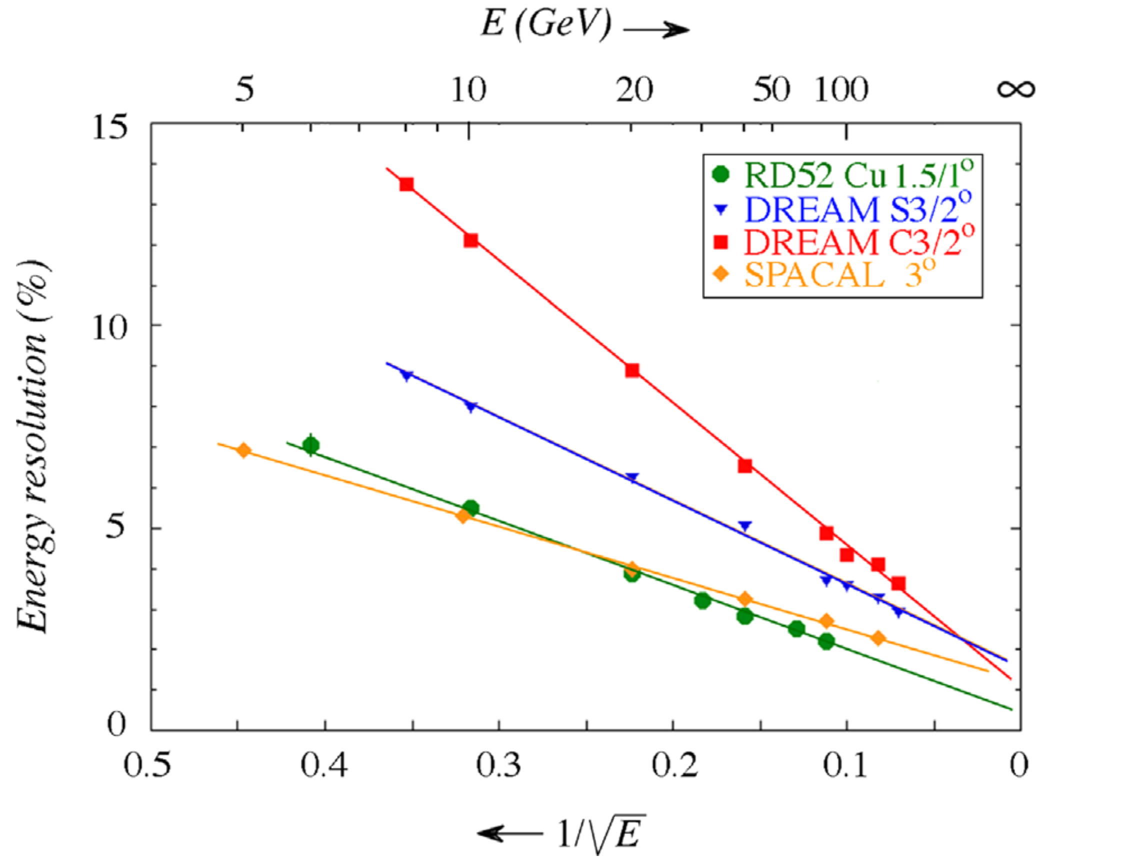

Fig. 22. Comparison of the em energy resolution measured with the RD52 copper-fiber calorimeter, the original DREAM copper-fiber calorimeter [3], and the SPACAL lead-fiber calorimeter [4].

2014

[27] NIM A 735 (2014) 120

- Particle identification in the longitudinally unsegmented RD52 calorimeter

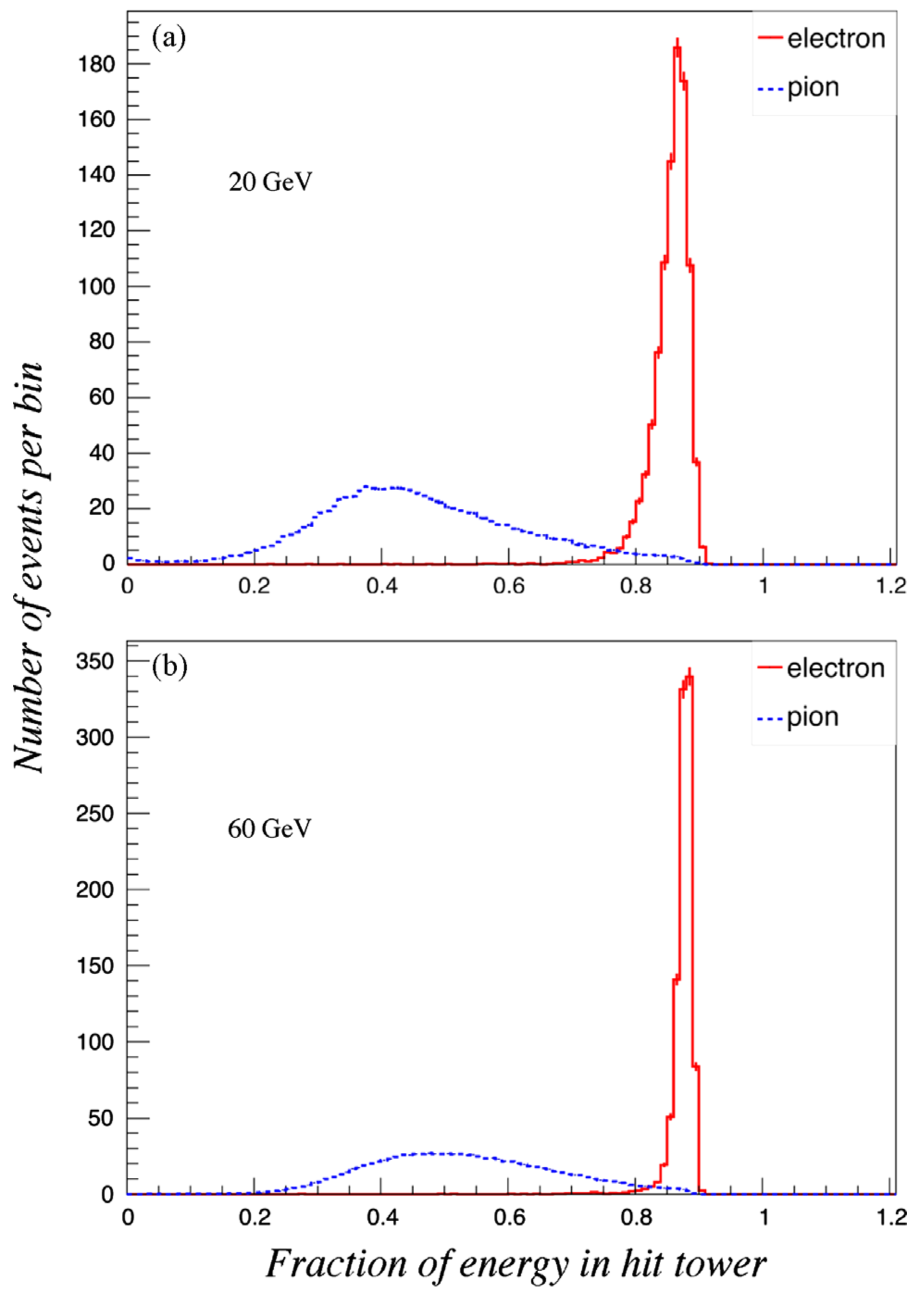

Fig. 6. Distribution of the energy fraction deposited in the hit tower by electrons and pions showering in the RD52 calorimeter. Data for 20 GeV (a) and 60 GeV (b) beam particles.

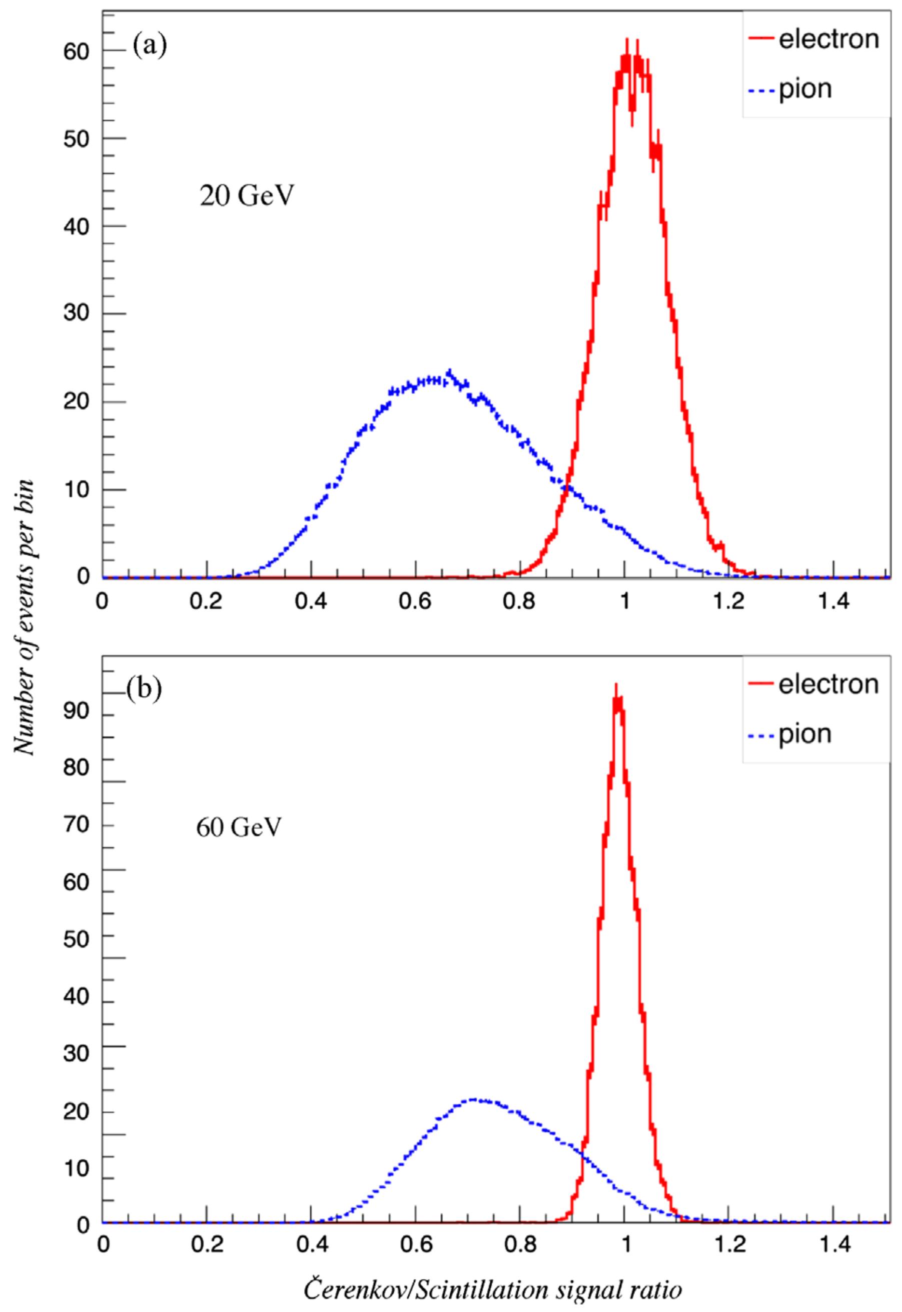

Fig. 7. Distribution of the C/S signal ratio in the hit tower for electrons and pions showering in the RD52 calorimeter. Data for 20 GeV (a) and 60 GeV (b) beam particles.

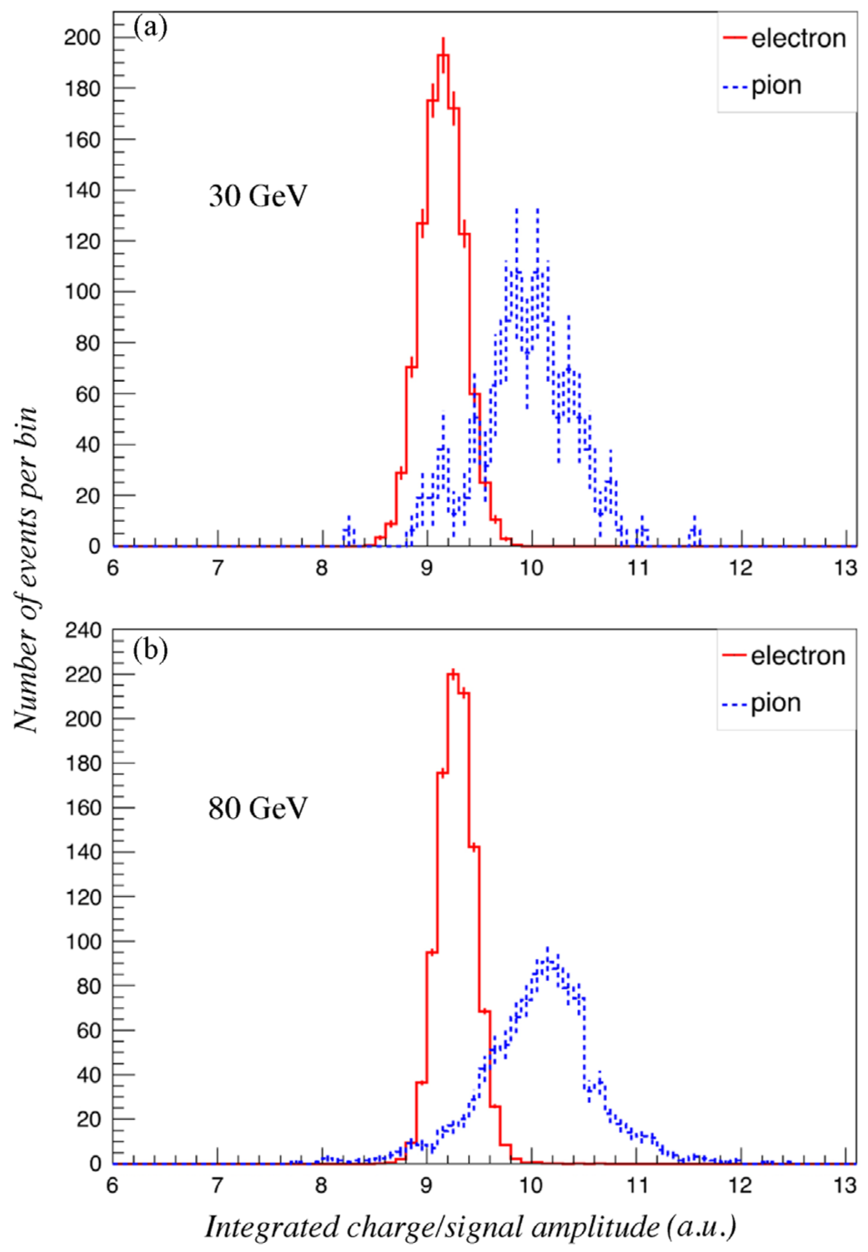

Fig. 11. Distribution of the ratio of the integrated charge and the amplitude of the signals produced by electrons and pions in one module of the RD52 fiber calorimeter. Data for 30 (a) and 80 GeV (b).

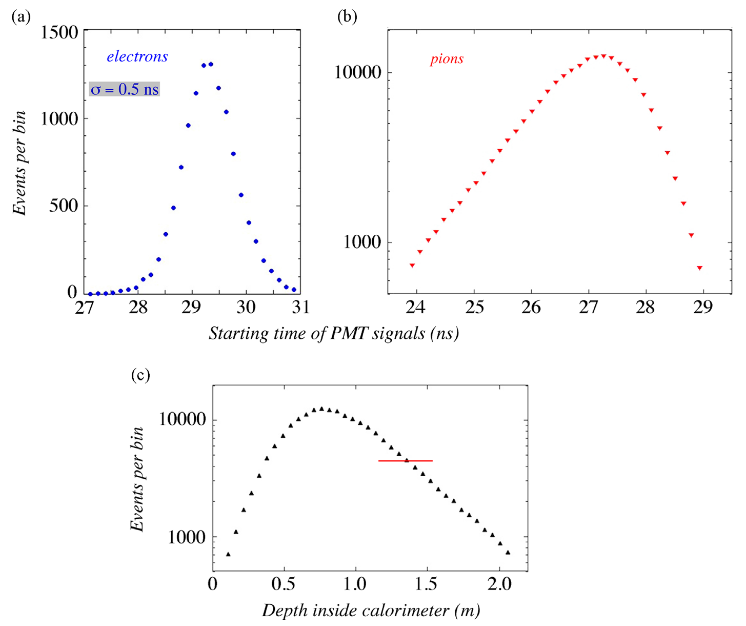

Fig. 9. The measured distribution of the starting time of the calorimeter's scintillation signals produced by 60 GeV electrons (a) and 60 GeV pions (b). This time is measured with respect to the moment the beam particle traversed trigger counter T1, installed upstream of the calorimeter (see Fig. 4). These data were used to determine the distribution of the average depth at which the light was produced in the hadron showers (c).

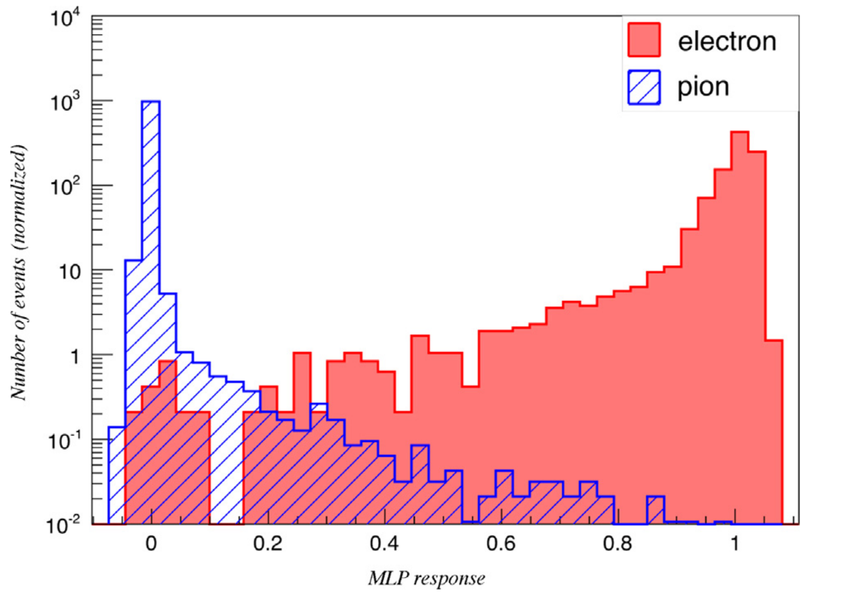

Fig. 12. Results from the multivariate analysis of the electron/pion separability at 60 GeV, which made simultaneous use of the lateral shower profile, the Cherenkov/scintillation signal ratio and the starting time of the PMT signals as the event characteristics that allowed distinguishing electrons from pions. The multi-layer perception (MLP) response indicates that 99.8% of all electrons could be identified with a combination of criteria that rules out 99.8% of all pions as electron candidates.

2014

[28] NIM A 762 (2014) 100

- Lessons from Monte Carlo simulations of the performance of a dual-readout fiber calorimeter

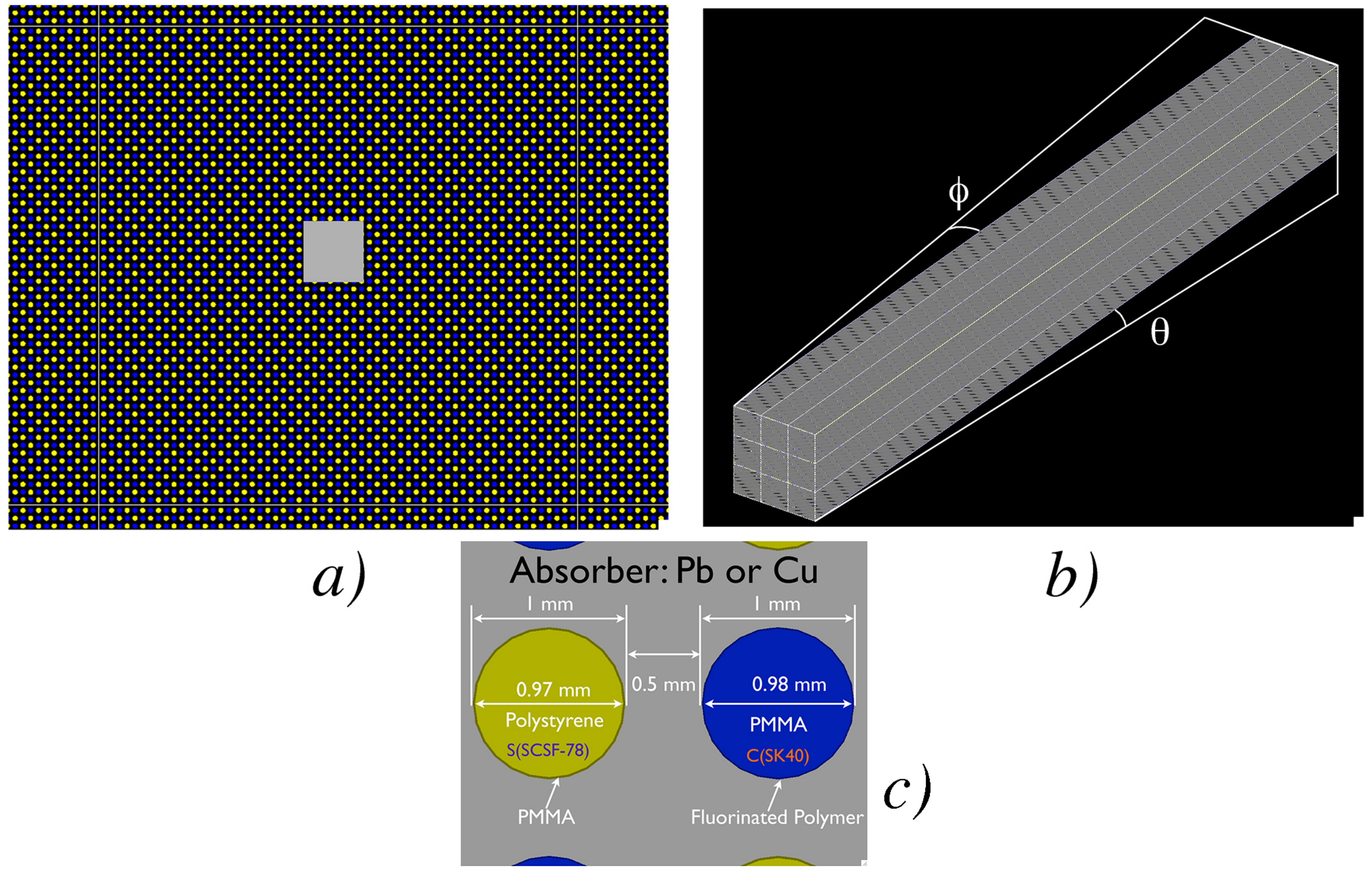

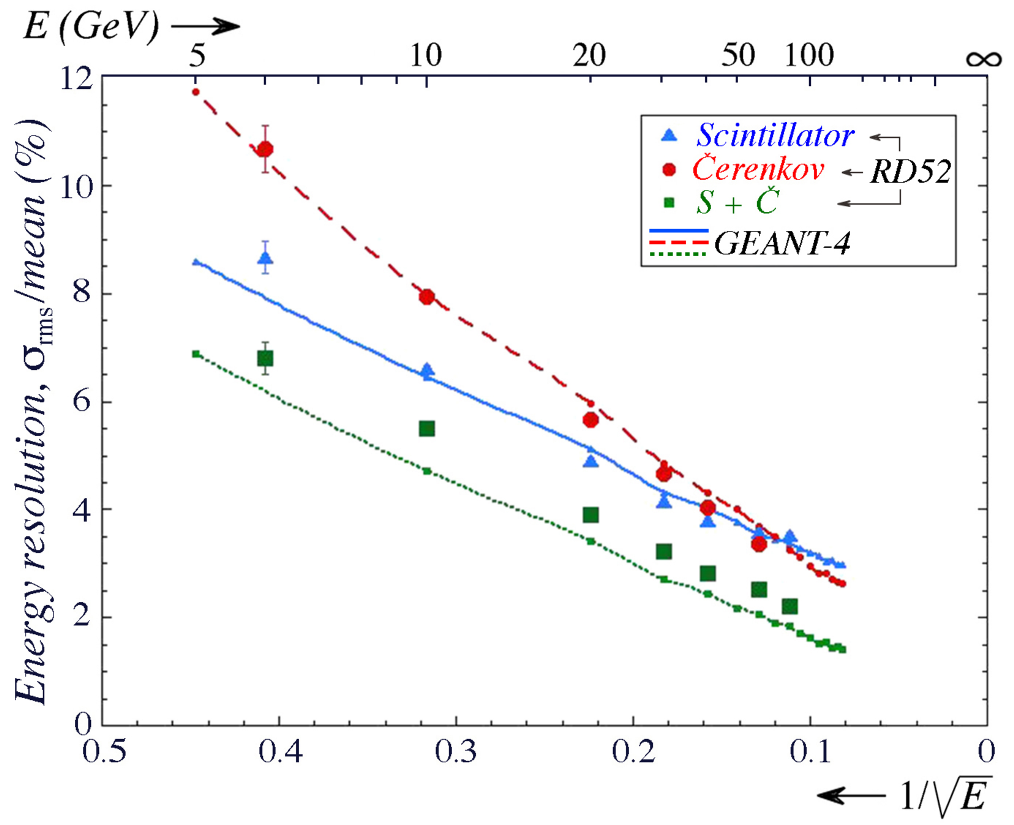

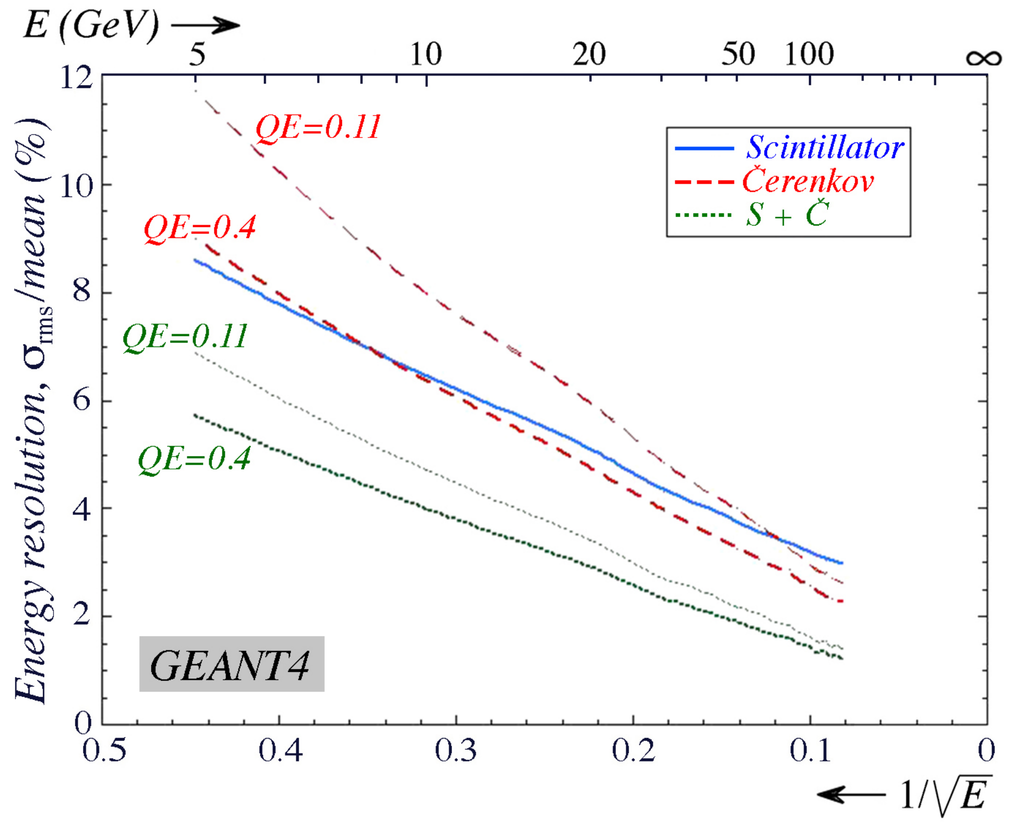

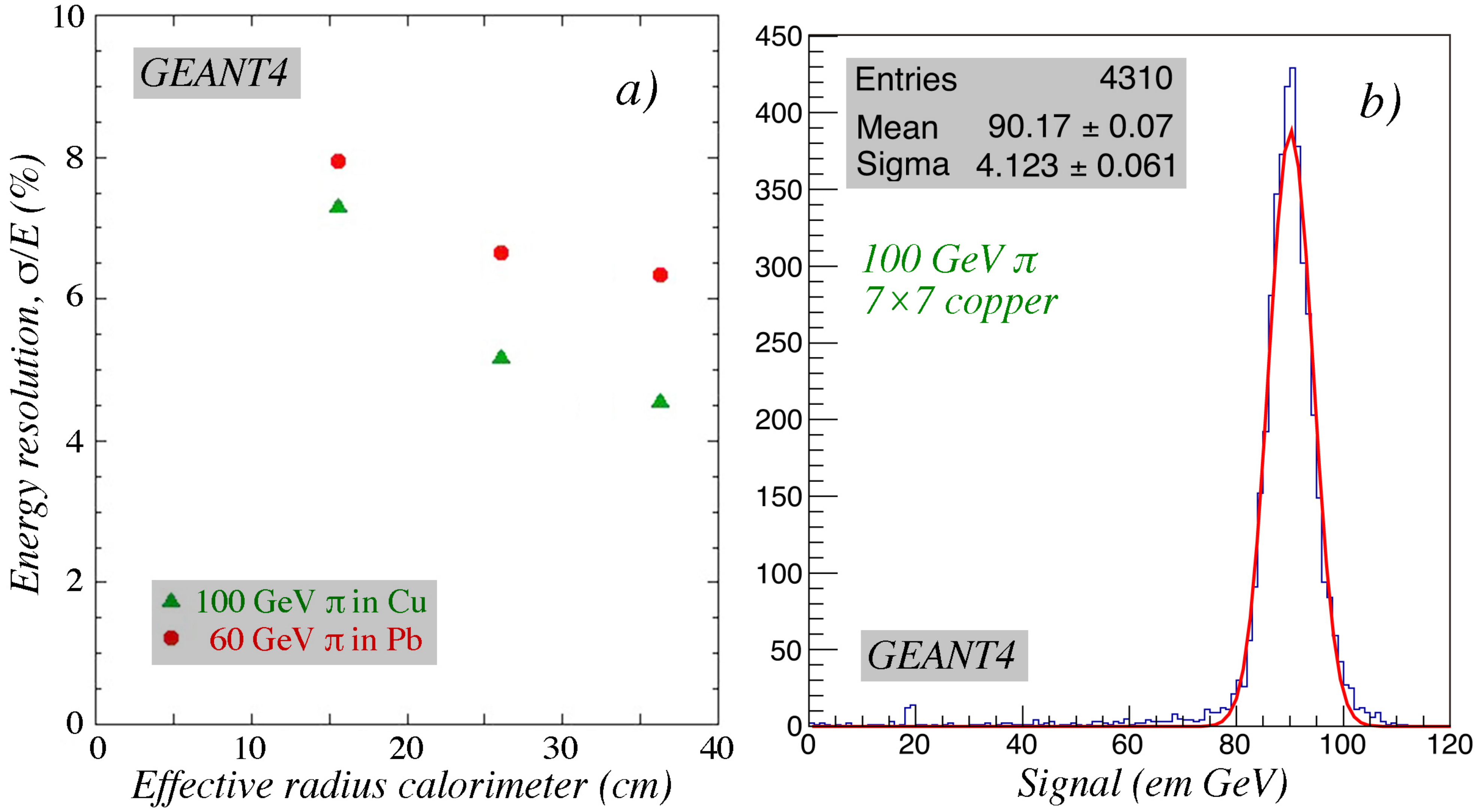

2017

[31] NIM A 866 (2017) 76

- Hadron detection with a dual-readout fiber calorimeter

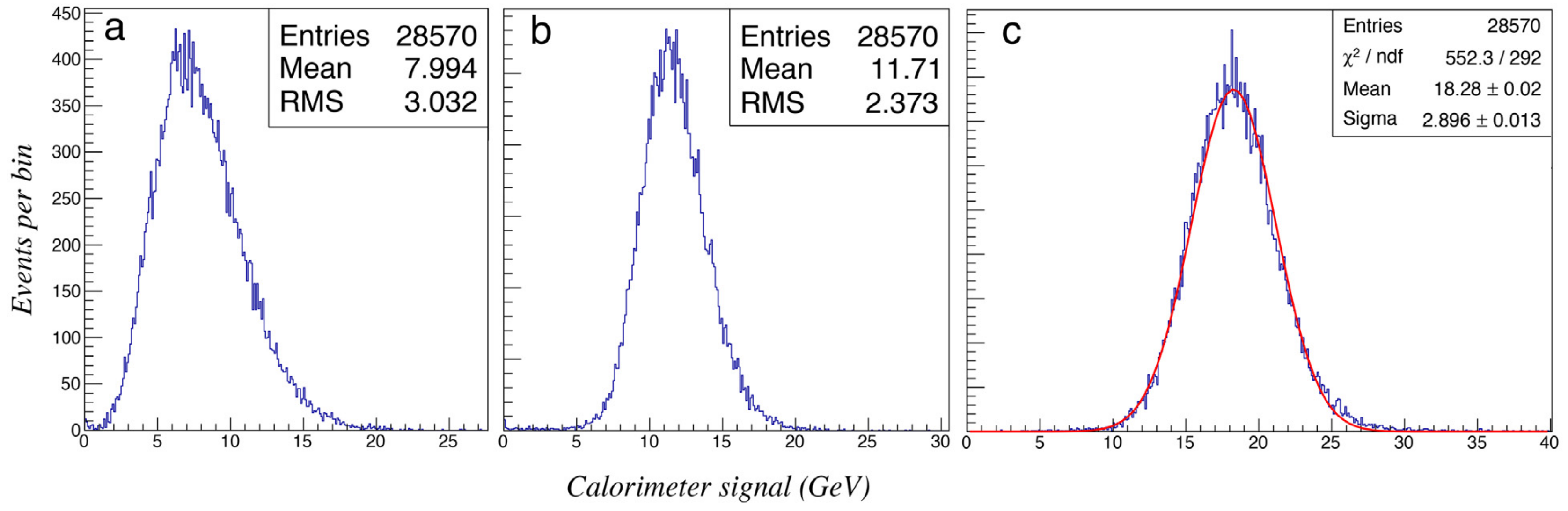

Fig. 11. Signal distributions for 20 GeV π^- particles. Shown are the measured Čerenkov (a) and scintillation (b) signal distributions as well as the signal distribution obtained by combining the two signals according to Eq. (2), using $\chi = 0.45$ (c).

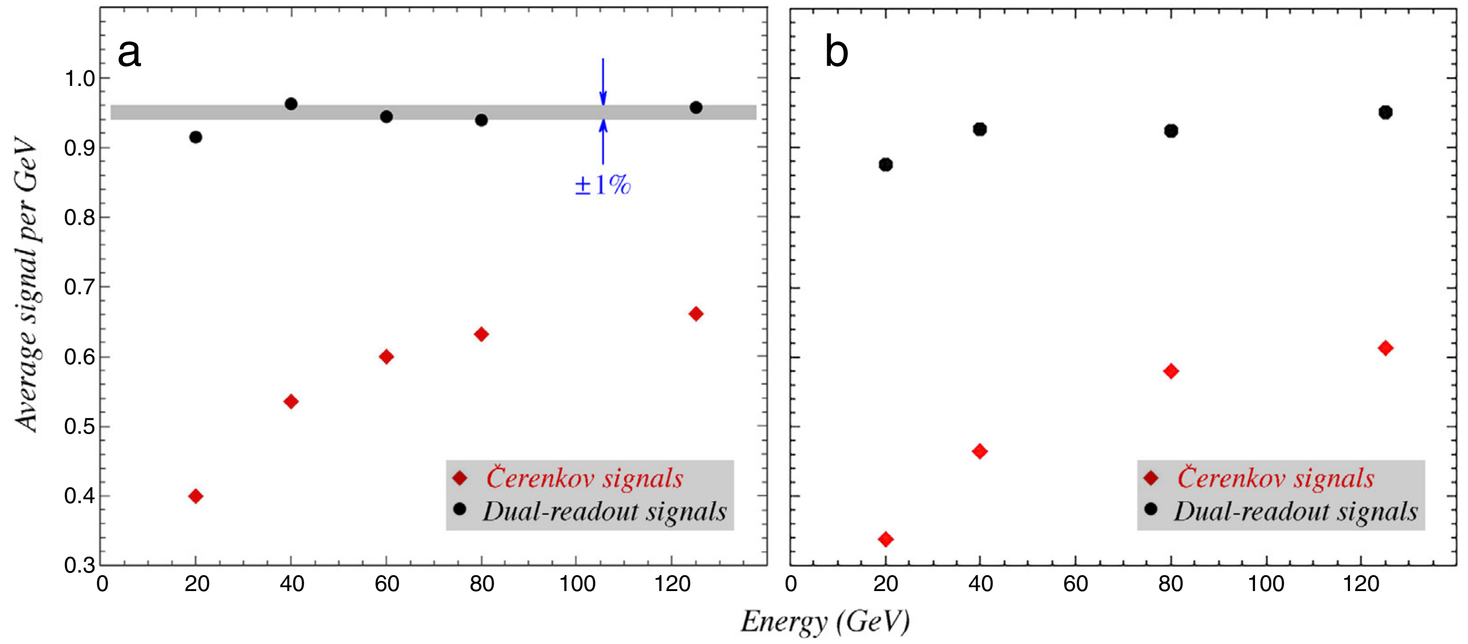

Fig. 12. The hadronic response of the RD52 lead–fiber dual-readout calorimeter, for single pions (a) and protons (b). Shown are the average Čerenkov signal and the dual-readout signal (Eq. (2)) per unit deposited energy, as a function of the energy.

$$E = \frac{S - \chi C}{1 - \chi}, \quad \text{with} \quad \chi = \frac{\left[1 - (h/e)_S\right]}{\left[1 - (h/e)_C\right]} \approx 0.3.$$

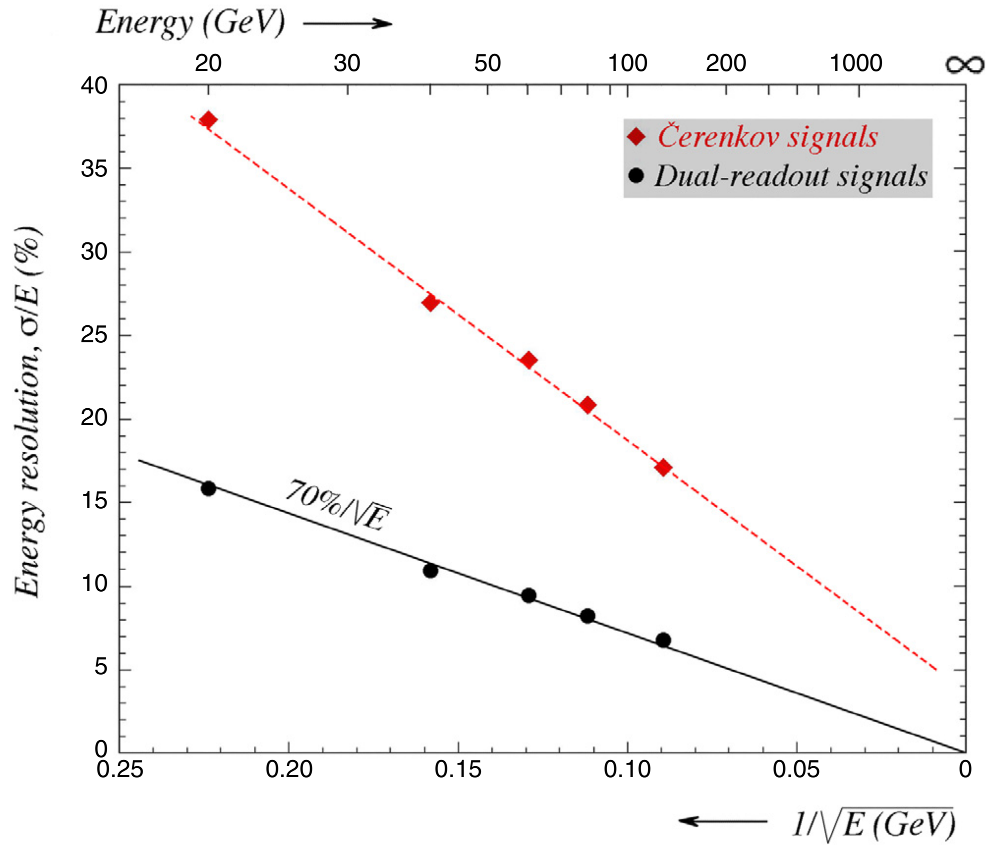

Fig. 13. The hadronic energy resolution of the RD52 lead–fiber dual-readout calorimeter, for single pions. Shown are the results for the Čerenkov signals alone, and for the dual-readout signals, obtained with Eq. (2).

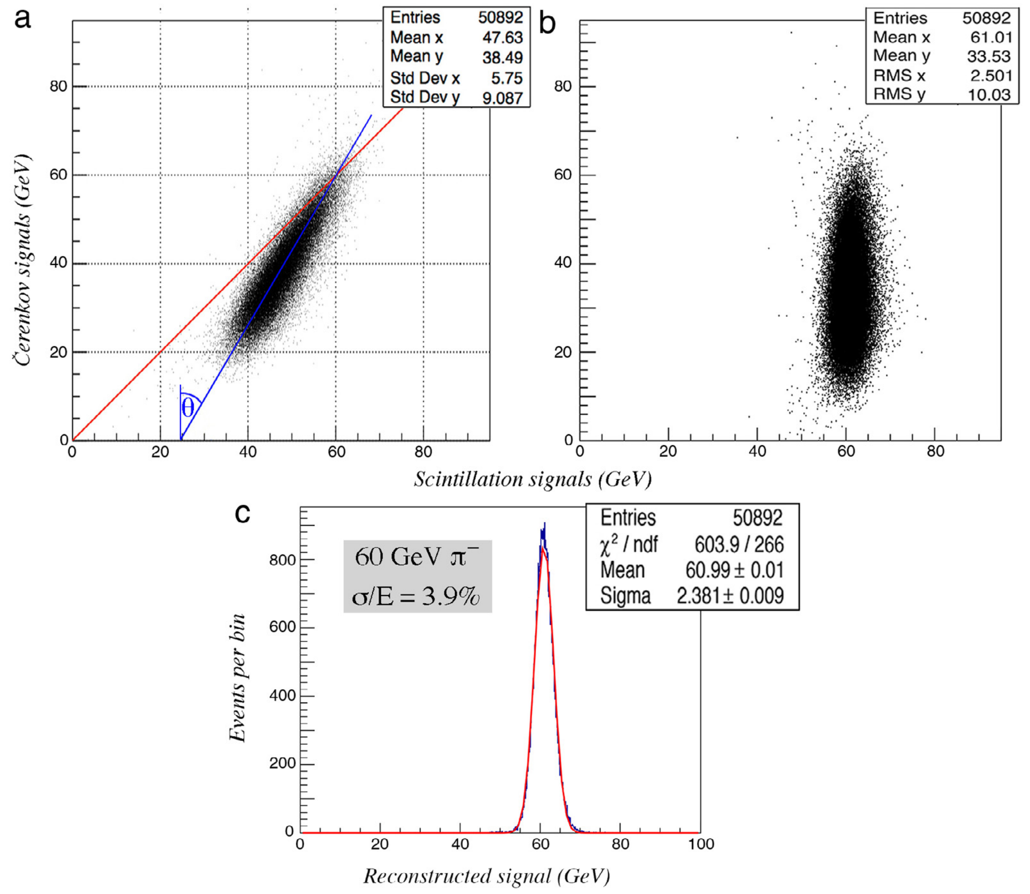

Fig. 14. Signal distributions of the RD52 Dual-Readout lead/fiber calorimeter for 60 GeV pions. Scatter plot of the two types of signals as recorded for these particles (a) and rotated over an angle $\theta = 30°$ around the point where the two lines from diagram a intersect (b). Projection of the latter scatter plot on the x-axis (c).

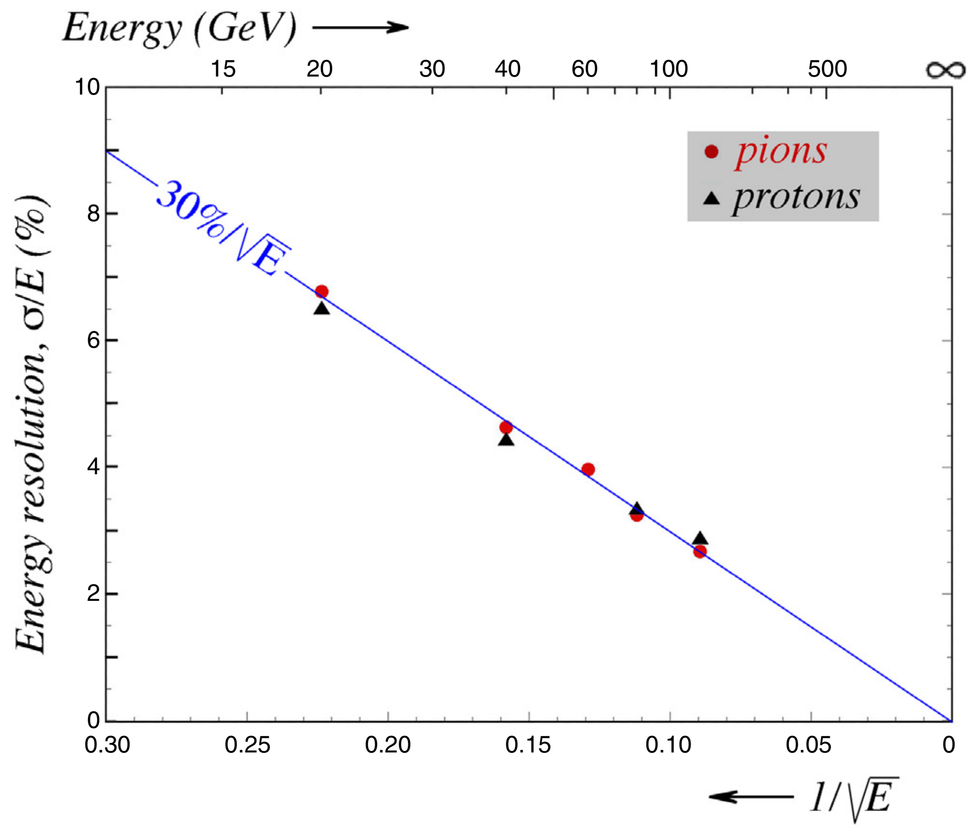

Fig. 18. The fractional width of the signal distribution, σ/E, as a function of energy, for pions and protons in the 20–125 GeV energy range. The line represents $\sigma/E = 30\%/\sqrt{E}$.

2018

[31] NIM A 882 (2018) 148

- On the limits of the hadronic energy resolution of calorimeters

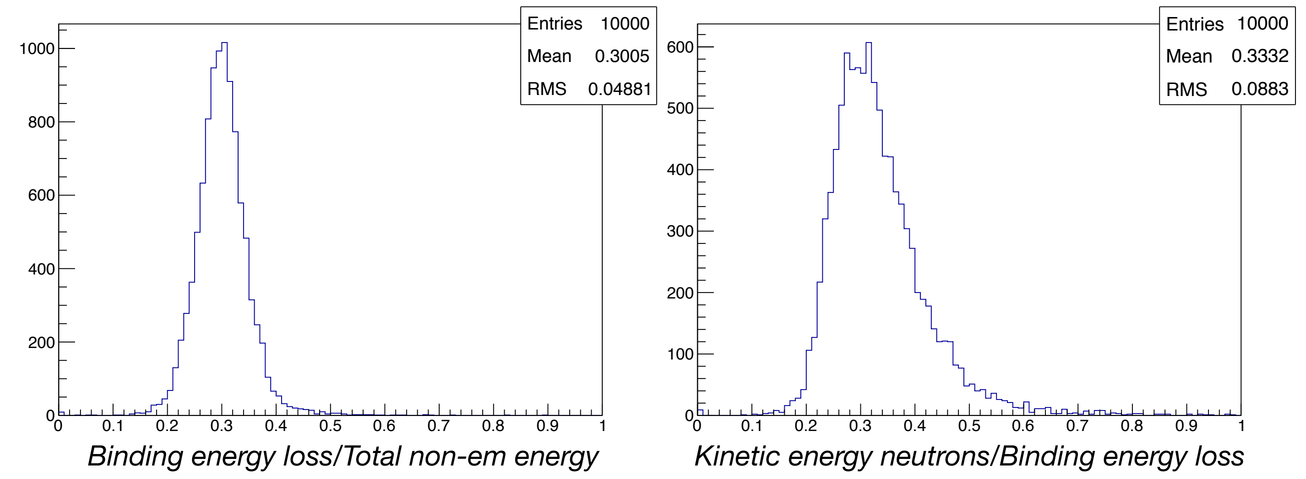

Figure 7. Correlations between the binding energy loss and the total non-em energy (left), and the neutron kinetic energy (right) for hadron showers produced with 20 GeV pions.

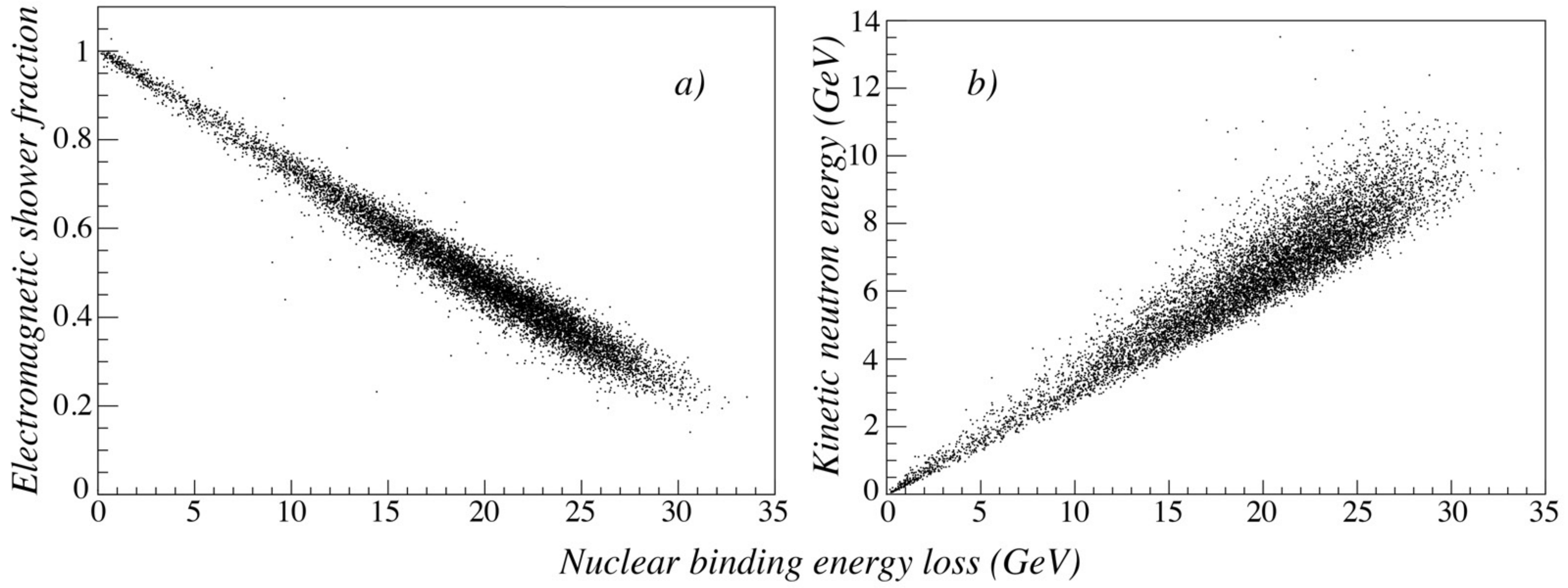

Figure 6. The correlations between the binding energy loss and the em shower fraction (a), and the neutron kinetic energy (b) obtained from GEANT 4 simulation in the case that 100 GeV pions produce hadron showers in the lead absorber.

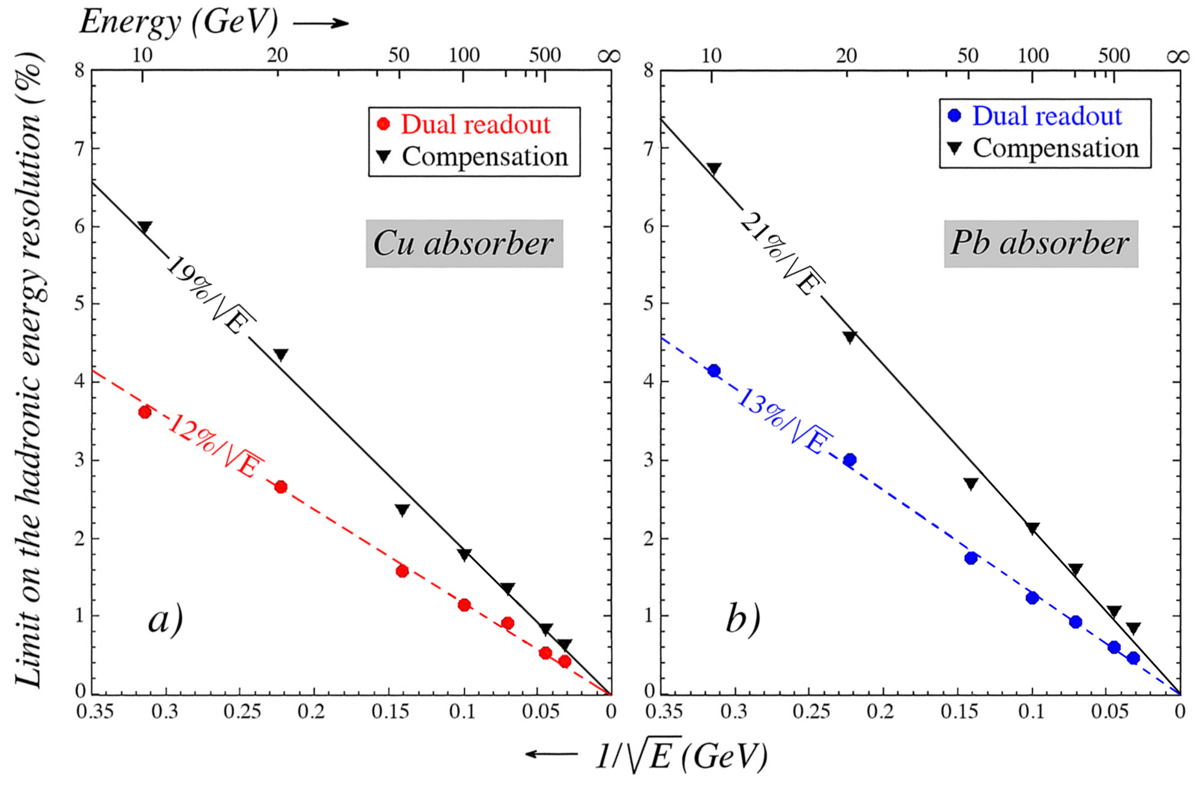

Figure 9. The limits of the hadronic energy resolutions for dual-readout and compensation obtained by the simulations with pion showers developing in Cu (a) and Pb (b) absorbers.

2018

[35] Rev. Mod. Phys. 90 (2018) 025002

- Dual-Readout Calorimetry
- Summarized 20 years R&D results

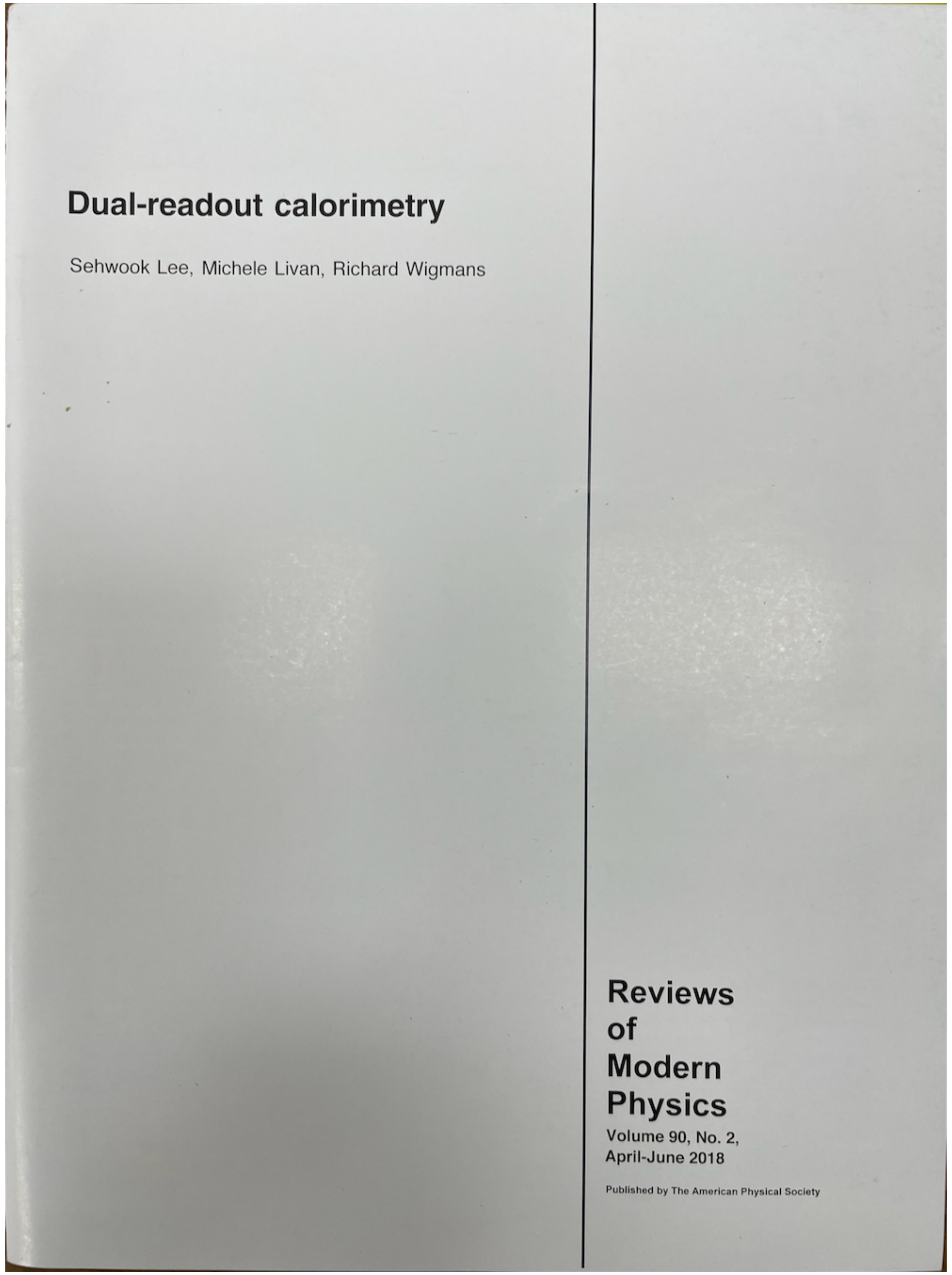

2009

LoI 4th concept for ILC: John Hauptman (Iowa State U.), et al.

- Pixel chamber + Cluster-timing drift chamber + Dual-Readout Calorimeter + Dual Solenoid (Iron Free) +

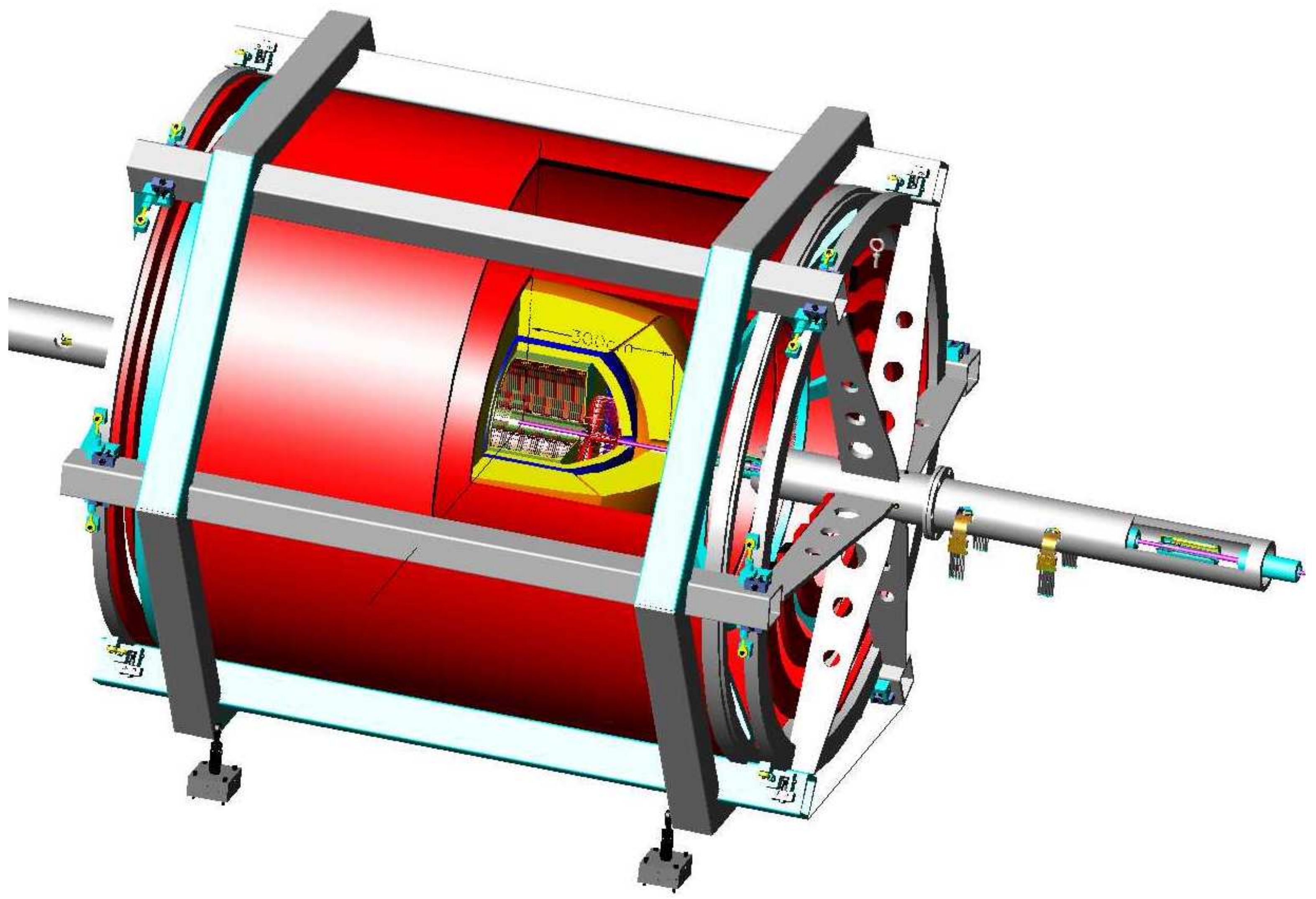

Figure 1: The 4th detector showing final focus transport, the dual solenoids for iron-free flux return, the vertex and tracking systems, and the calorimeters in yellow: inner one is dual-readout crystal and outer is dual-readout fiber, both with time history readout. The total depth is 10 λ_I and all calorimeter channels are projective with the origin. The frame is non-magnetic and easily able to contain the magnetic pressure $\propto B^2$. The gross dimensions are 12 meters in diameter and 16 meters long, excluding the beam delivery.

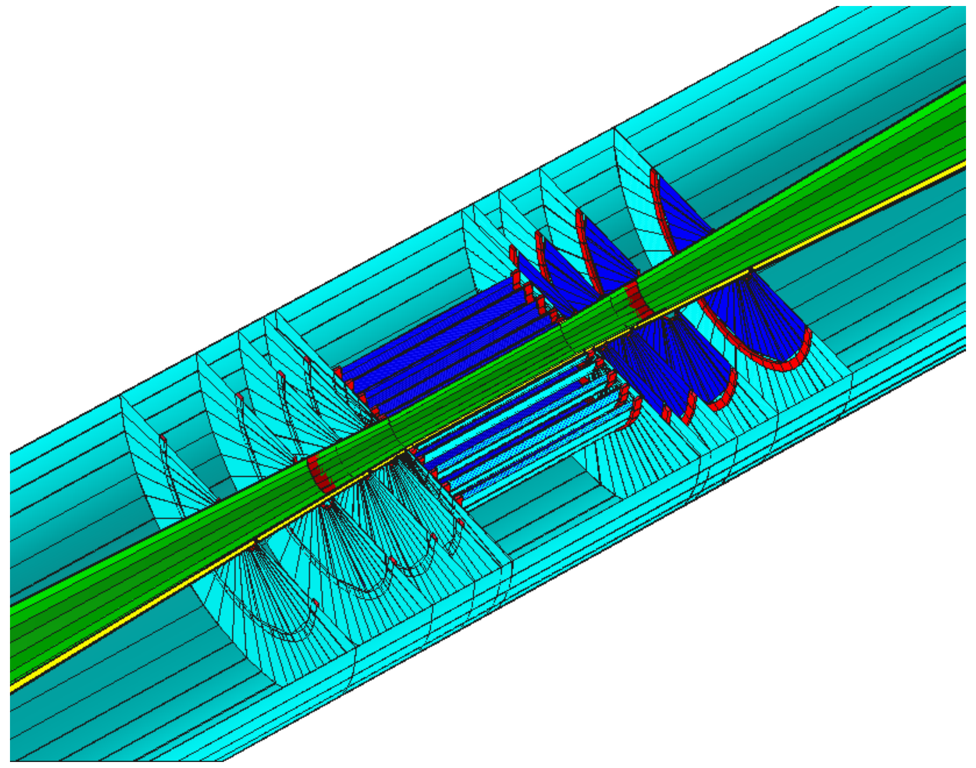

Figure 2: The vertex detector as simulated in ILCroot.

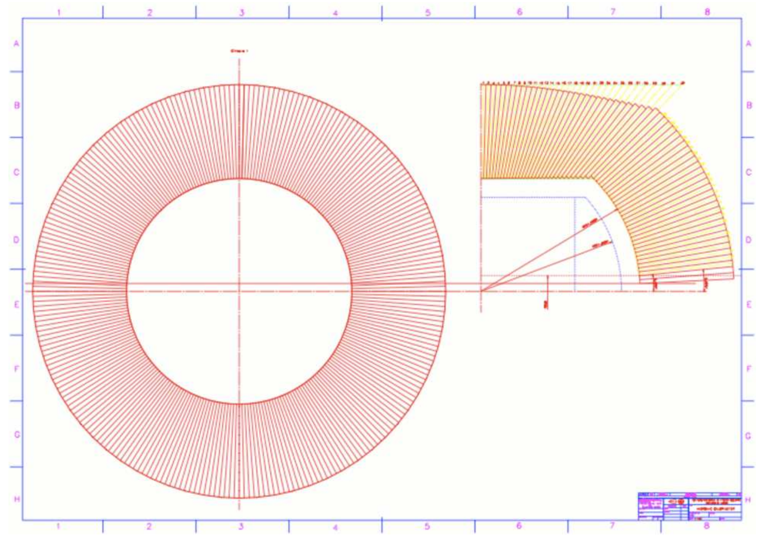

Figure 22: Azimuthal segmentation of the hadronic calorimeter at $z = 0$. There are 256 towers in each of the 32 slices in θ. At left the $r - z$ projection, where one can see the segmentation of 32 concentric tower arrangements of the end cap. In blue are the contours of the CluCou chamber. The space between the chamber and the fiber calorimeter is filled with the crystal (EM) calorimeter.

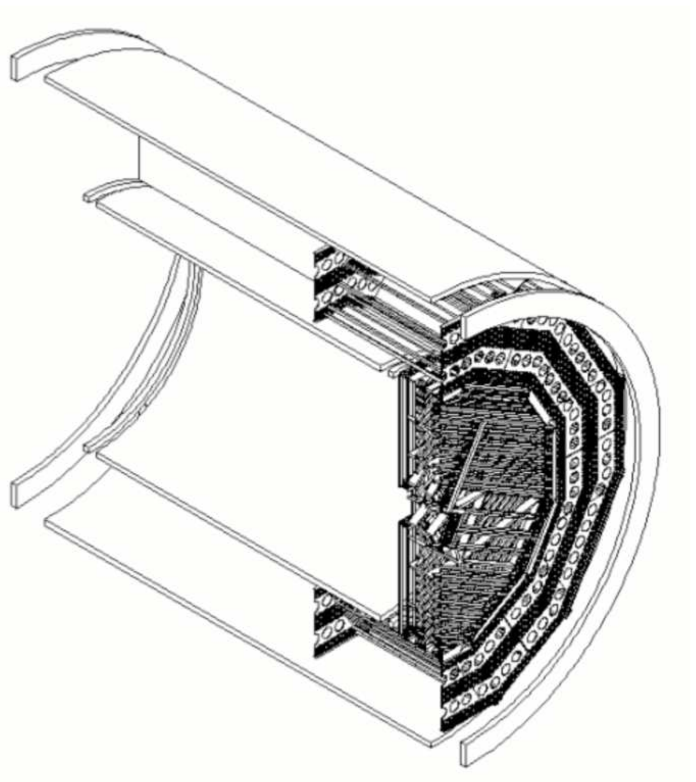

Figure 31: Schematic view of one stave of the barrel muon spectrometer and one end cap. Only a few tubes have been drawn.

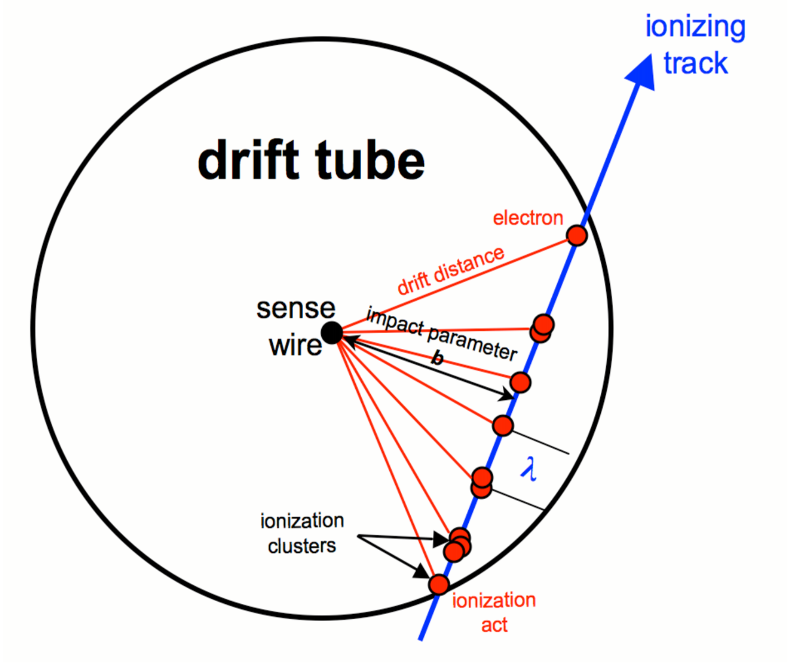

Figure 5: Schematization of the cross view of a drift tube with the definitions used in the text.

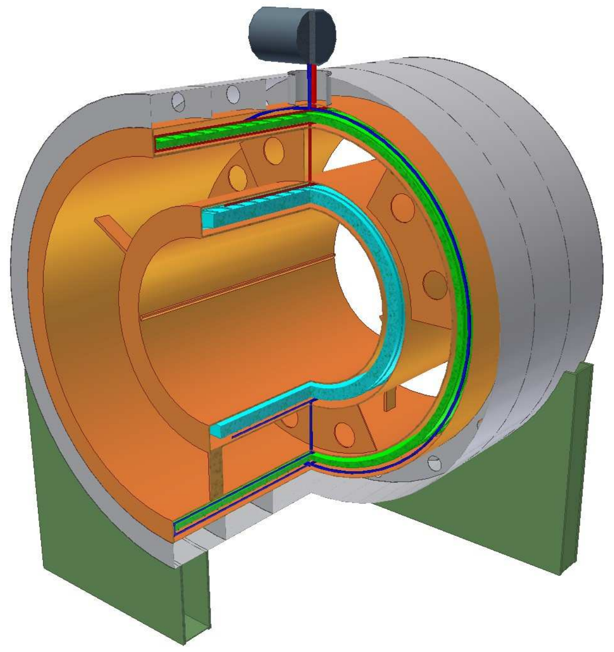

Figure 24: Cut view of the two solenoids and their supports.

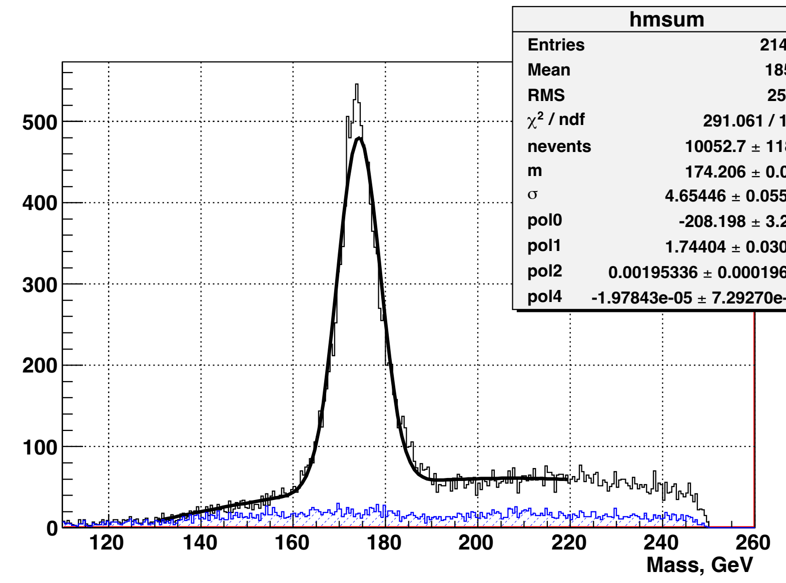

t quark mass reconstructed with standard model backgrounds.

2016

The First Hong Kong meeting at HKUST for CEPC

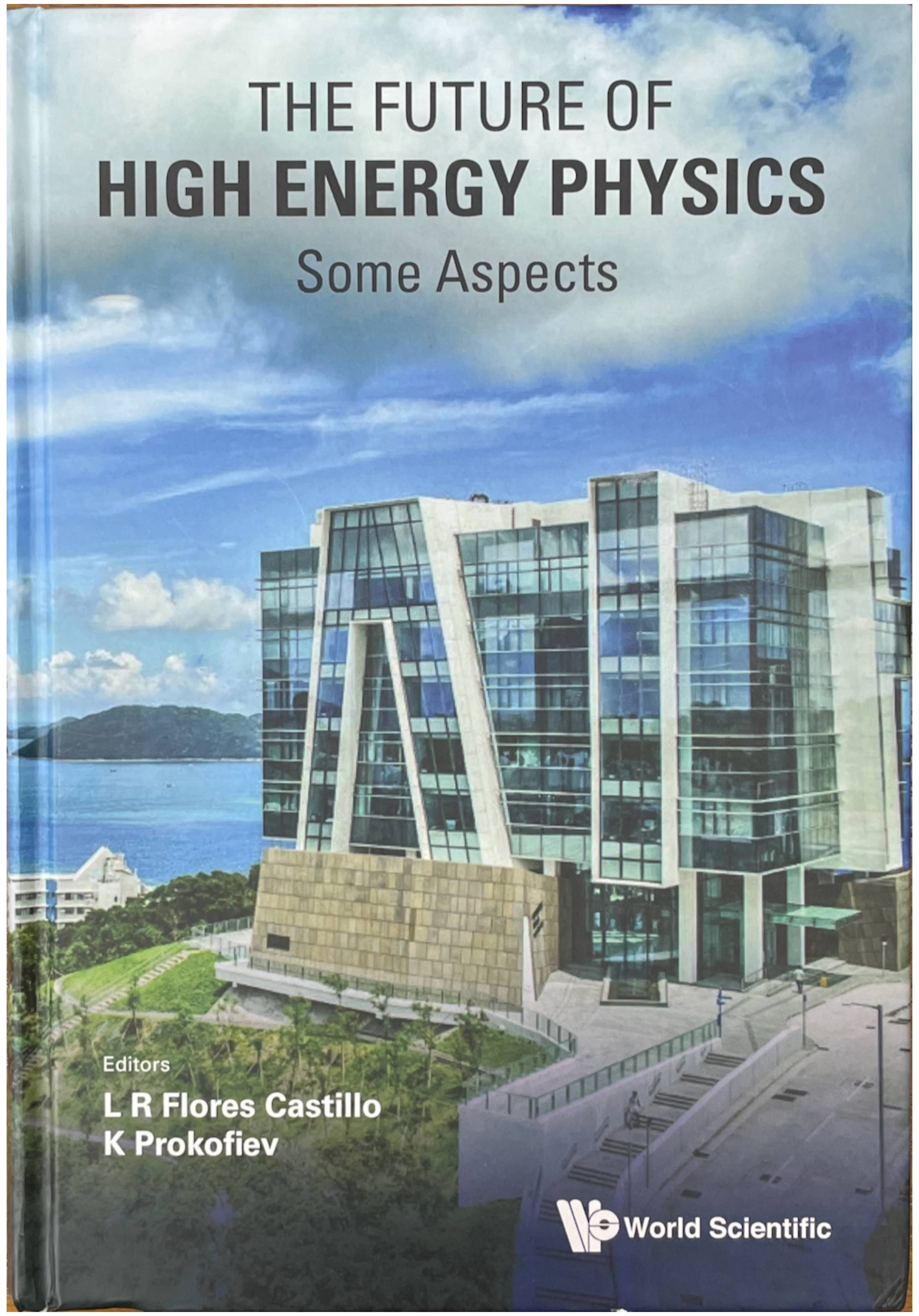

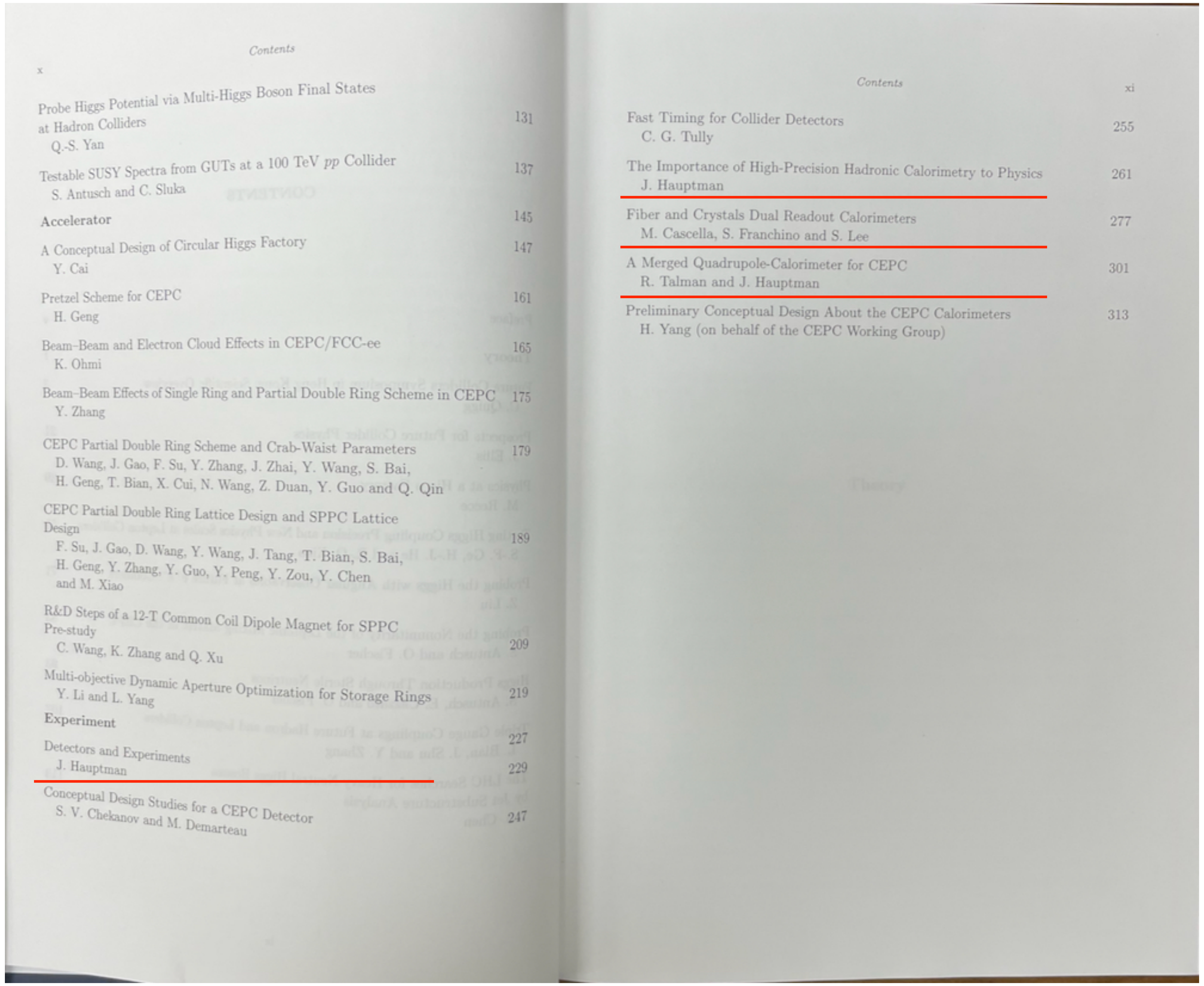

2018

FCC-ee and CEPC CDRs

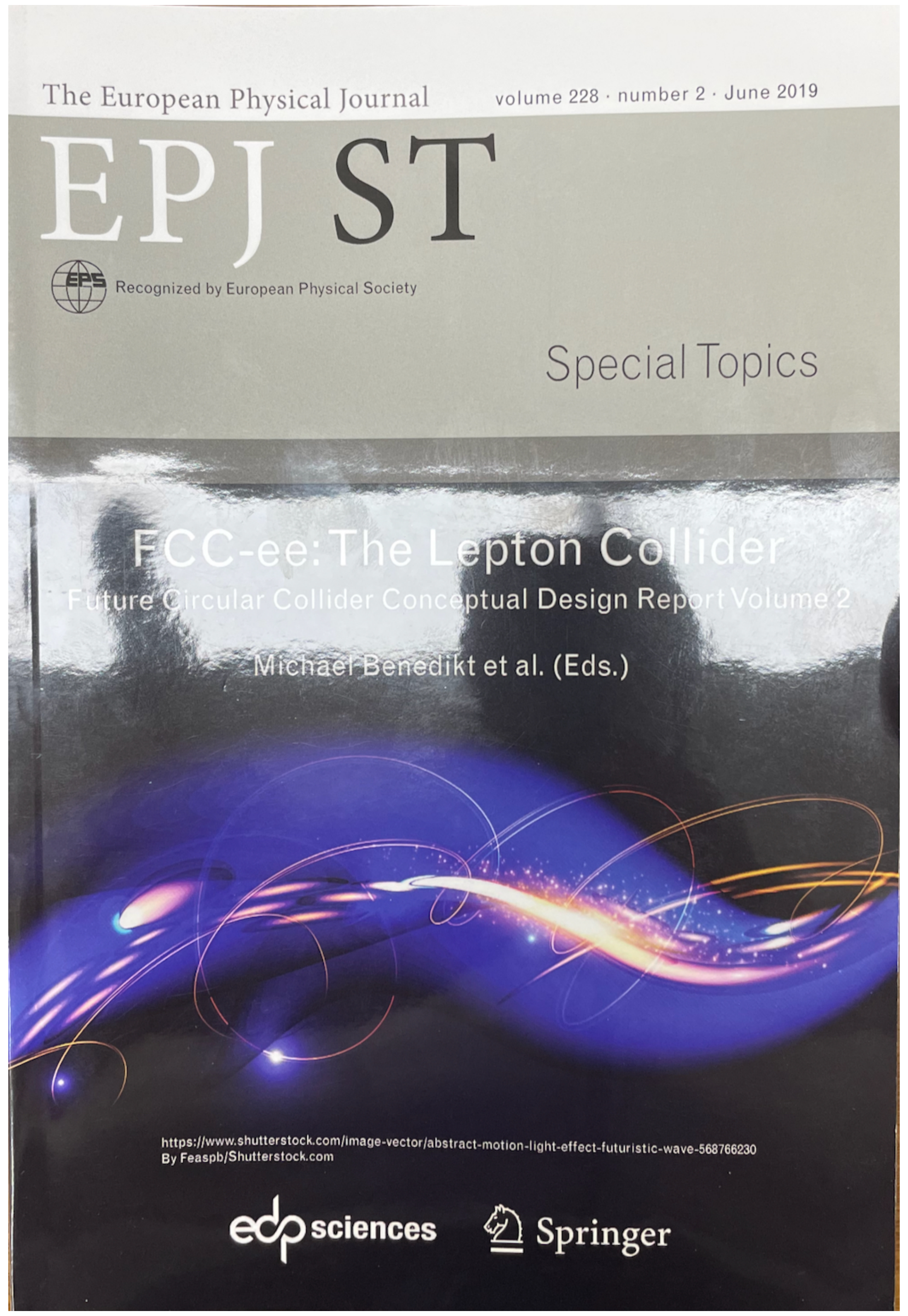

A. Kulesza[344], M. Kumar[56], M. Kumar[328], A. Kusina[99], S. Kuttimalai[225], M. Kuze[239], T. Kwon[216], F. Lackner[64], M. Lackner[284], E. La Francesca[115,271], M. Laine[289], G. Lamanna[152], S. La Mendola[64], E. Lançon[20], G. Landsberg[21],

W.-M. Yao[160], E. Yazgan[97], V. Yermolchik[95], A. Yilmaz[112], A. Yilmaz[75], H.-D. Yoo[216], S.A. Yost[234], T. You[298], C. Young[225], T.-T. Yu[318], F. Yu[141], A. Zaborowska[64], S.G. Zadeh[320], M. Zahnd[57], M. Zanetti[129,267], L. Zanotto[116],

264 The European Physical Journal Special Topics

T. Lari[126], P.J. Laycock[308], P. Lebrun[65], A. Lechner[64], K. Lee[216], S. Lee[24,151], R. Lee[23], T. Lefevre[64], P. Le Guen[64], T. Lehtinen[201], S.B. Leith[279], P. Lenzi[123,262],

IHEP-CEPC-DR-2018-02

IHEP-EP-2018-01

IHEP-TH-2018-01

CEPC

Conceptual Design Report

Volume II - Physics & Detector

The CEPC Study Group

October 2018

Zihang Jia[37], Jiechen Jiang[26], Yun Jiang[88], Jianbin Jiao[46], Dapeng Jin[26,221], Mingjie Jin[26], Shan Jin[37], Song Jin[26], Yanli Jin[26], Yi Jin[61], Maoqiang Jing[26,62], Hyunsuk Jo[222], Jaya John[167], Tim Jones[165], Xudong Ju[26], Adil Jueid[47], Sunghoon Jung[134], Susmita Jyotishmati[214], Goran Kacarevic[147],

Tetsuya Kobayashi[130], Panyu Kong[55], Shibei Kong[26], Joachim Kopp[97], Ashutosh Kotwal[182], Jonathan Kozaczuk[189], Evgeny A. Kozyrev[144], Alexander Krasnov[153], Eric Kuflik[107], Taeun Kwon[134], Chia-Ming Kuo[158], King Wai Kwok[103], Francois Lagarde[47], Pei-Zhu Lai[158], Imad Laktineh[94],

Jingbo Ye[209], Mei Ye[26,221], Qiang Ye[26], Ziping Ye[186], Fang Yi[26,60], Kai Yi[192], Xue Yilun[37], Hang Yin[6], Pengfei Yin[26], Xiangwei Yin[26], Ze Yin[81], Zhongbao Yin[6], Hwi Dong Yoo[134], Zhengyun You[57], Charles Young[208], Boxiang Yu[26,221], Chenghui Yu[26], Chunxu Yu[39], Dan Yu[26], Felix Yu[97], Fusheng Yu[34],

Chia-Ming Kuo[158], King Wai Kwok[103], Francois Lagarde[47], Pei-Zhu Lai[158], Imad Laktineh[94], Boyang Lan[55], Xiaofei Lan[13], Lia Lavezzi[128,26], Kyeongpil Lee[134], Sehwook Lee[222], Seung J. Lee[136], Ge Lei[26], Yongbin Leng[28], Sze Ching Leung[204], Bingzhi Li[47], Bo Li[68], Bo Li[26], Boyang Li[59],

International Collaboration

Prof. Hyonsuk Jo (KNU)
Prof. Yongsun Kim (Sejong U.)
Prof. Jason Lee (UoS)
Prof. Sehwook Lee (KNU)
Prof. Hwidong Yoo (YU)

Korea

Prof. Rong-Shyang Lu

Prof. Chia Ming Kuo

Taiwan

Japan

Prof. Yuji Enari
(Active from 2021)

DREAM FOR FUTURE

USA

Prof. Sarah Eno

Prof. Chris Tully

Prof. Richard Wigmans

Prof. John Hauptman

Europe

Prof. Paolo Giacomelli (Bologna)
Prof. Romualdo Santoro (Insubria)
Prof. Roberto Ferrari (Pavia)
Prof. Franco Bedeschi (Pisa)

Prof. Iacopo Vivarelli

Prof. Valery Chmill

Full-size prototype detector

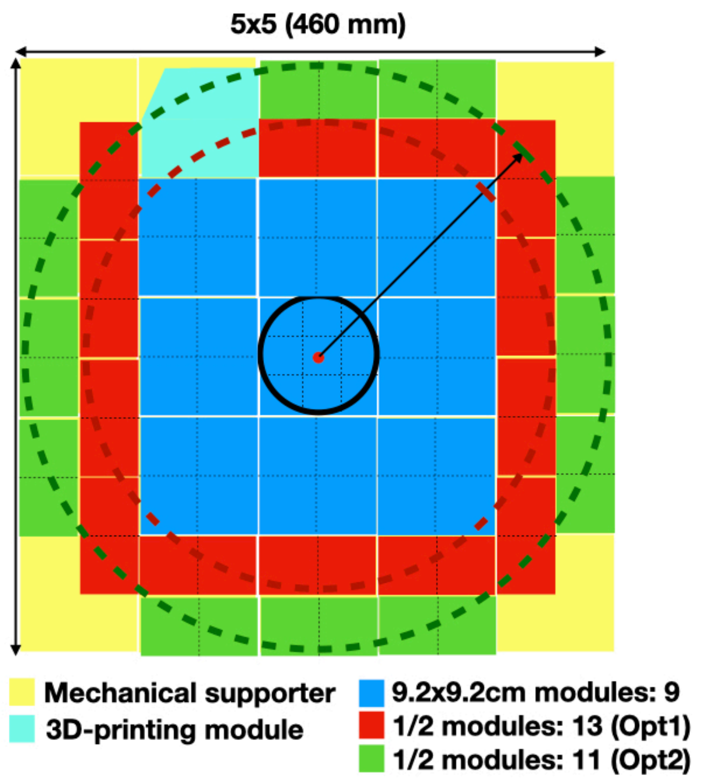

DRC with crystal

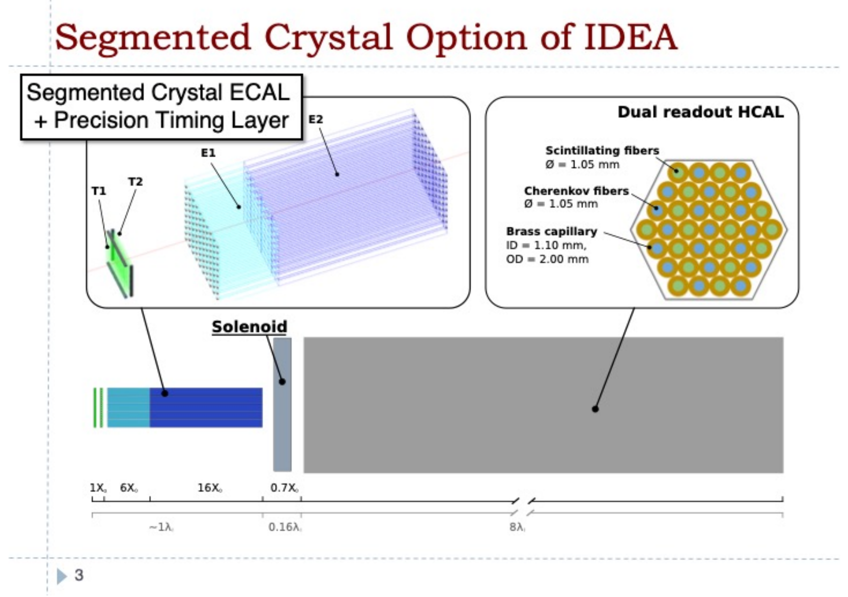

Bucatini prototype

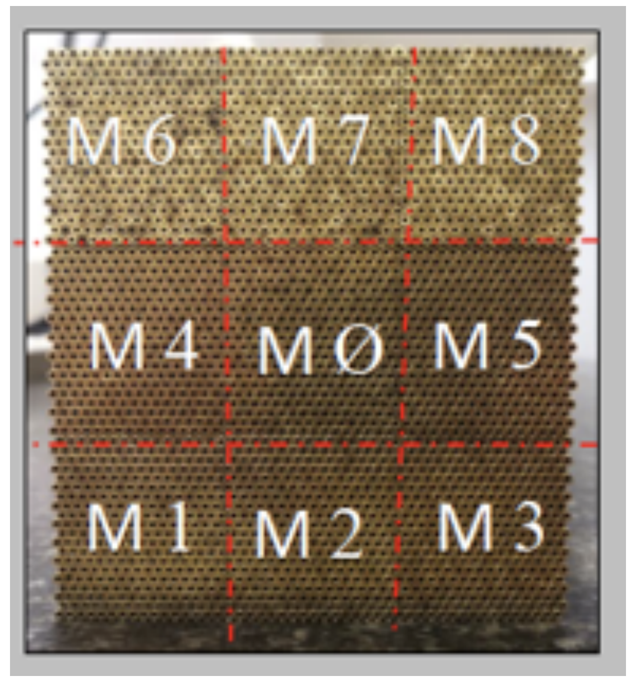

International collaboration forms

- Regular meeting
- Compensated R&D options
- Combine efforts

Conclusion

Experience, Colleagues, Passion